energies

MDPI

Article

A Comparison of Frequency-Dependent Soil Models: Electromagnetic Transient Analysis of Overhead Transmission Lines Using Modal Decomposition

Tainá Fernanda Garbelim Pascoalato [1,*], Anderson Ricardo Justo de Araújo [2], Jaimis Sajid Leon Colqui [2], Sérgio Kurokawa [1] and José Pissolato Filho [2]

[1] Department of Electrical Enegineering, São Paulo State University (UNESP), Ilha Solteira 15385-000, Brazil; sergio.kurokawa@unesp.br
[2] School of Electrical and Computer Engineering, State University of Campinas (UNICAMP), Campinas 13083-852, Brazil; ajaraujo@unicamp.br (A.R.J.d.A.); jeimis.leon@gmail.com (J.S.L.C.); pisso@unicamp.br (J.P.F.)
* Correspondence: tfg.pascoalato@unesp.br

Abstract: This article investigates the influence of four causal frequency-dependent (FD) soil models and their impact on the responses of a multiphase overhead transmission line (OHTL) with ground wires, generated by a lightning strike. The FD models proposed by Longmire-Smith (LS), Messier (M), Portela (P) and Alípio-Visacro (AV) are considered. The ground-return impedance and admittance matrices are computed with the Nagakawa approach for both frequency-constant and FD soil models. The frequency-domain modal voltages and time-domain transient voltages are assessed in this work. Modal decomposition technique is used to study the attenuation constant, propagation velocity and voltages for each propagation mode. Simulations are carried out in a frequency range of 100 Hz to 10 MHz, for OHTLs with lengths of 1 and 10 km, on soils of 700 and 4000 Ω·m. Simulation results demonstrated that the Portela (P) model has resulted in more significant variation in the ground-return impedance and admittance, constant attenuation and propagation velocity in which a pronounced variation, especially at the high frequencies, is seen. On the other hand, Longmire-Smith (LS) and Messier (M) have produced similar results in both frequency and time domains. Additionally, the Alípio-Visacro (AV) model has produced intermediate responses, being the model recommended by CIGRÈ WG C4.33. Time-domain induced voltage waveforms obtained with the Portela (P) model has shown pronounced differences, especially at the peak values, for the high-resistive soil. This study demonstrates the importance of considering the FD soil models to assess the transient responses adequately, especially when OHTLs are on high-resistive soils.

Keywords: electromagnetic analysis; lightning; multiphase overhead lines; modal decomposition; frequency-dependent soil models

Citation: Garbelim Pascoalato, T.F.; Justo de Araújo, A.R.; Leon Colqui, J.S.; Kurokawa, S.; Pissolato Filho, J. A Comparison of Frequency-Dependent Soil Models: Electromagnetic Transient Analysis of Overhead Transmission Lines Using Modal Decomposition. *Energies* **2022**, *15*, 1687. https://doi.org/10.3390/en15051687

Academic Editors: Andrea Bonfiglio, Issouf Fofana and Andrea Mazza

Received: 28 January 2022
Accepted: 22 February 2022
Published: 24 February 2022

1. Introduction

Accurate modeling of OHTLs is required to study the electromagnetic transients on power systems, especially for those generated by lightning strikes [1,2]. OHTLs are characterized by its FD distributed parameters where the voltage and current behave as propagating waves. To calculate the transient responses on a certain OHTL, the solving methods can be classified into two categories [3]: (1) phase-domain methods and (2) modal-domain methods. In (1), the fitting techniques in the *s*-plane requires an accurate calculation of travelling time τ of the OHTLs for frequency-domain characteristic admittance $Y_c(\omega)$ and propagation wave function $H(\omega)$ functions to properly calculate the time-domain responses as detailed in [4–6]. Additionally, the traditional Universal Line Model (ULM), depending on the fitting process in the rational-function approximation, may require a high computation time, being this an important factor in the real time simulators [7]. In (2), the transient responses are dependent of transformation matrices that can be obtained by different algorithms [3,8,9]. Besides that, the FD soil electrical parameters can be included in the FD longitudinal impedance $\boldsymbol{Z}_{\ell}(\omega)$ and FD transversal matrices $\boldsymbol{Y}_{\mathrm{t}}(\omega)$. However, the modal-domain variables require frequency-to-time domain conversion methods such as inverse Laplace/Fourier transforms.

Regarding the FD parameters of a transmission line, the ground-return impedance and ground-return admittance of a certain OHTL located on a lossy soil must be carefully evaluated [2,10–13]. In this context, Carson was the first author to consider the effect of ground-return currents on a OHTL located on this type of ground [14] in 1926. Carson computed the ground-return impedance considering the soil modeled by only a frequency-independent conductivity (σ_{g}), and neglected both displacement currents [2,13,14]. Ground is not a perfect conductive medium, and the potential at the surface of the ground is not expected to be equal to zero at the high frequencies [15]. Due to the electric field penetrating the ground, corrections on shunt admittances must be added, even though these factors might be small. On this basis, Nakagawa in [15] provided a more realistic approach for the ground-return impedance and admittance matrices. In his assumptions, the soil is modeled as a homogeneous semi-infinite plane conductor where displacement currents for several soil relative permittivities ε_{r} are considered. Nakagawa's approach allows that the FD soil electrical parameters-$\rho_{\mathrm{g}}(f)$ and $\varepsilon_{\mathrm{r}}(f)$ be included into his expressions. Several papers dealing with the complex integrals concerning the ground-return impedance and admittance based on numerical solutions or closed-form expressions are available in the literature [16–20].

Soil is characterized by its FD soil resistivity $\rho(f)$ and relative permittivity $\varepsilon_{\mathrm{r}}(f)$ and the constant magnetic permeability μ which is assumed to be equal to the vacuum magnetic permeability μ_0 [21]. In the literature, many authors have proposed different closed-form expressions based on the soil samples collected in field and laboratory measurements [22,23]. It is demonstrated that when the soil models are considered, the transient voltage peaks on OHTL are significantly reduced in comparison to those computed for the frequency-constant soil [1,24]. Accuracy on voltage peaks is necessary to compute the electrical supportability of many components in power systems such as insulator strings, pre-insertion resistors, circuit breakers and surge arresters [1,2].

This article investigates the impact of four causal FD soil models proposed in the literature (Longmire-Smith, Messier, Portela and Alípio-Visacro) and on the transient responses generated on a 440-kV OHTL with two ground wires subjected to a lightning strike. For this analysis, modal decomposition is employed where three independent single-phase lines are studied in the frequency-domain. The ground-return impedance and admittance matrices are computed by the classical Nakagawa's approach for frequency-constant and four causal FD soil models. Simulations are carried out in a frequency range of 100 Hz to 10 MHz, considering two OHTLs with lengths of 1 and 10 km located on soils of 700 and 4000 $\Omega\cdot$m. The transient voltage generated for a current is representative of a lightning subsequent return stroke. Results demonstrated that when FD soil models are assumed, the ground-return impedance, admittance, constant attenuation and propagation velocity present pronounced variation, especially at the high frequencies and high-resistive soil obtained for the Portela (P) model. As a consequence, the phase-domain transient responses can have a significant impact on the voltage waveforms. Simulation results indicated that expressive reductions on the peaks of the induced voltages are obtained with the Portela (P) model, which is more pronounced for the high-resistive soil. This research indicates the importance of considering the FD soil models to assess the time-domain transient responses adequately on OHTL generated by high-frequency content phenomena.

As contribution, we considered that the effects of ground wires on the top of OHTL are included by using the Kron's method where a reduced ground-return impedance and admittance matrices are obtained. Then, the modal decomposition technique is applied to study the impact of FD soil models on the transient responses developed for a lightning strike. Besides that, a more complete approach for ground-return impedance and admittance matrices using the Nakagawa's formulations are studied in this work. All the programming codes developed can be incorporated in any simulation platforms or extended to the main EMP-type programs.

The rest of the paper is organized as follows: In Section 2, a literature review on the main papers related to the OHTL modeling including the ground-return impedance and admittance are presented. In Section 3, the modeling of a multiphase OHTL focusing on the ground-return impedance and admittance proposed by Nakagawa is provided. In Section 4, the closed-form expressions for four causal soil models are described. In Section 5, the modal decoupling of an OHTL is presented. In Section 6, the ground wires reduction is detailed. In Section 7, the numerical results concerning the proper OHTL on FD soils are discussed. Finally, in Section 8, the main conclusions of the paper are summarized.

2. Literature Review

In the recent years, proper soil modeling applied on OHTL under distinct types of disturbances has received a lot of attention from researchers.

Some papers consider the FD σ_g and ε_r during line energization (switching maneuver which is a low-frequency content phenomenon) such as [10,25,26]. De Conti et al. in [12] analyzed the transient responses on 3.6 km single and bi-phase distribution lines neglecting the overhead ground wire located on a high-resistive soil (10,000 Ω·m). In [27], Moura et al. analyzed the influence of the FD soils in terms of the p.u.l. longitudinal impedance and transversal admittance for a single-circuit 345-kV OHTL with two ground wires. In [28], Moura et al. studied the voltages generated for the same 345-kV OHTL with two ground wires using the lightning current modeled as ramp of 1.2/50 μs in ATP-software for distinct soil models. De Conti et al. in [29], presented the transient responses generated for a lightning strike on two different single and bi-phase OHTLs located on soils of 100, 1000 and 10,000 Ω·m with lengths of 0.6 km and 1.8 km in which the overhead ground wires were neglected. The modal decomposition was used where the FD soil parameters and ground-return admittance had a significant impact on the transient responses. In [30], considering a set of measurements, He et al. investigated the impact of the frequency effect on σ_g and ε_r on the line parameters of 500-kV OHTL with two ground wires using the complex return plane method. However, the analysis does not extend to the time-domain responses.

In [24], Schroeder et al. compute the transient voltages generated for a 138-kV OHTL with one ground wire located on distinct soil models employing the ATP-software. For this analysis, the phase conductors and ground wires are represented by LINE CONSTANTS routine where the JMarti's line model was employed to compute the line parameters. In this program, the ground-return impedance is calculate by Carson's approach and the ground-return admittance is neglected. Papadopoulos et al. in [8] investigated the impact of many ground-return approaches (Carson, Dubanton, Noda, Pettersson, Wise) combined with the FD soil model of Longmire-Smith (LS) on the constant attenuation and transient voltages at the open-receiving end with distinct overhead distribution lines without ground wires. Diniz et al. in [2] investigate the influence of the ground-return admittance using the Pettersson's formulation using the Alípio-Visacro (AV) FD model on OHTLs of 138-kV with one ground wire and 230-kV with two ground wires. Only the ground mode is investigated in the modal decomposition.

Martins-Britto et al. [31] based on the work of Tsiamitros et al. [32] proposed a technique to approximate a multilayer soil by a homogeneous soil to calculate the ground-return impedance using the Nakagawa's approach in a frequency range of 1 Hz to 2 MHz. Then, the transient voltages are calculated and studied in the ATP software for 150-kV single circuit three-phase OHTL with neutral wires. Zanon et al. [33] uses ULM developed directly in the phase domain implemented in the ATP software for 230-kV and 115-kV three-phase distribution lines located on frequency-constant and FD soil parameters. A summary regarding some of the recent articles are described in Table 1.

Table 1. Comparison between some articles in the literature and the proposed work.

Article	Line Type	Soil Model (Constant/FD)	Ground Wires	Ground Admittance	Numerical Method	Modal Domain?	Type of Disturbance
Martins-Britto [31]	150-kV single-circuit 3ϕ	FD	Yes	No	ATP	No	Fault
Diniz [2]	138-kV/230-kV single-circuit 3ϕ	FD	Yes Yes	Yes	NILT	Yes	Lightning/ Switching
Conti [29]	1ϕ, 2ϕ single-circuit	FD	No	Yes	ATP	Yes	Lightning/ Switching
Zanon [33]	230-kV-3ϕ 115-kV-3ϕ	constant/ FD	Yes No	No	ULM	No	Switching
Papadopoulos [8]	3ϕ	FD	No	Yes	Codes in MATLAB	Yes	Switching
Moura [27]	345-kV single-circuit 3ϕ	FD	Yes	No	ATP	No	Lightning
Proposed work	440-kV single-circuit 3ϕ	FD	Yes	Yes	NILT	Yes	Lightning

Based on the above mentioned works and Table 1, modal decomposition technique is an interesting tool to compute the transient OHTL with overhead ground wires located on soils with FD electrical parameters. As expected, the four causal FD soil models will have a significant impact on the transient responses generated by lightning. These responses are evaluated in the modal domain where distinct frequency-dependent variables such as propagation velocity ($v_{\mathrm{m}}(\omega)$), constant attenuation ($\lambda_{\mathrm{m}}(\omega)$), modal impedance ($Z_{\mathrm{m}}(\omega)$), modal admittance ($Y_{\mathrm{m}}(\omega)$) and modal voltages ($V_{\mathrm{m}}(\omega)$) are analysed. Then, on the phase domain, the time-dependent currents and voltages and their behaviour can be properly visualized during the electromagnetic transient state and interpreted based on the results from the modal domain.

3. Modeling of OHTLs

OHTLs are characterized by the longitudinal impedance $\boldsymbol{Z}_{\ell}(\omega)$ and transversal admittance $\boldsymbol{Y}_{\mathrm{t}}(\omega)$ matrices, in per-unit-length, given by

$$\boldsymbol{Z}_{\ell}(\omega) = \boldsymbol{Z}_{\mathrm{i}}(\omega) + \boldsymbol{Z}_{\mathrm{e}}(\omega) + \boldsymbol{Z}_{\mathrm{g}}(\omega), \tag{1}$$

$$\boldsymbol{Y}_{\mathrm{t}}(\omega) = j\omega \boldsymbol{C}_{\mathrm{t}} = \left(\boldsymbol{Y}_{\mathrm{e}}^{-1}(\omega) + \boldsymbol{Y}_{\mathrm{g}}^{-1}(\omega)\right)^{-1}. \tag{2}$$

In (1), $\omega = 2\pi f$ [rad/s] is the angular frequency, f [Hz] is the frequency, $\boldsymbol{Z}_{\mathrm{i}}(\omega)$ [Ω/m] is the internal impedance due to the Skin effect [1], $\boldsymbol{Z}_{\mathrm{e}}(\omega)$ [Ω/m] is the external matrix due to other conductors above soil [34] and $\boldsymbol{Z}_{\mathrm{g}}(\omega)$ [Ω/m] is the ground-return impedance associated to the penetrating magnetic field resulting in the induced currents into the soil [14,35]. In (2), $\boldsymbol{C}_{\mathrm{t}}$ [F/km] is the equivalent transversal capacitance, $\boldsymbol{Y}_{\mathrm{e}}(\omega)$ [S/m] is the external admittance considering a constant parameter soil and $\boldsymbol{Y}_{\mathrm{g}}(\omega)$ [S/m] is the ground-return admittance corresponding to a correction term for FD soils. Ground-return impedance $\boldsymbol{Z}_{\mathrm{g}}(\omega)$ and the ground-return admittance $\boldsymbol{Y}_{\mathrm{g}}(\omega)$ must be precisely computed for the transient analysis. Nakagawa's approach (NA) is a classical formulation that includes the ground effect on the longitudinal impedance and on the transversal admittance [15]. In NA, the soil is modeled as a homogeneous semi-infinite plane conductor and considered displacement currents. The ground-return impedance ($\mathbf{Z}_\mathrm{g}(\omega)$) and the ground-return admittance ($\mathbf{Y}_\mathrm{g}(\omega)$) for this approach are given by [15]

$$Z_{\mathrm{g}_{\mathrm{ii}}}(\omega) = j\frac{\omega\mu_0}{\pi}\int_0^\infty \frac{e^{-2h_\mathrm{i}\lambda}}{\sqrt{\lambda^2 + j\omega\mu_0(\sigma_\mathrm{g} + j\omega(\varepsilon_\mathrm{r}-1)\varepsilon_0)}\frac{\mu_0}{\mu_\mathrm{g}} + \lambda}d\lambda, \tag{3}$$

$$Z_{\mathrm{g}_{\mathrm{ij}}}(\omega) = j\frac{\omega\mu_0}{\pi}\int_0^\infty \frac{e^{-(h_\mathrm{i}+h_\mathrm{j})\lambda}}{\sqrt{\lambda^2 + j\omega\mu_0(\sigma_\mathrm{g} + j\omega(\varepsilon_\mathrm{r}-1)\varepsilon_0)}\frac{\mu_0}{\mu_\mathrm{g}} + \lambda}\cos(r_\mathrm{ij}\lambda)d\lambda, \tag{4}$$

$$\mathbf{Y}_\mathrm{g}(\omega) = j\omega\mathbf{P}_\mathrm{g}^{-1}(\omega), \tag{5}$$

being

$$P_{\mathrm{g}_{\mathrm{ii}}}(\omega) = \frac{1}{\pi\varepsilon_0}\int_0^\infty \frac{e^{-2h_\mathrm{i}\lambda}}{\left(\frac{\lambda\gamma_\mathrm{g}^2}{\gamma_0^2} + \sqrt{\lambda^2 + j\omega\mu_0(\sigma_\mathrm{g} + j\omega(\varepsilon_\mathrm{r}-1)\varepsilon_0)}\right)}d\lambda, \tag{6}$$

$$P_{\mathrm{g}_{\mathrm{ij}}}(\omega) = \frac{1}{\pi\varepsilon_0}\int_0^\infty \frac{e^{-(h_\mathrm{i}+h_\mathrm{j})\lambda}}{\left(\frac{\lambda\gamma_\mathrm{g}^2}{\gamma_0^2} + \sqrt{\lambda^2 + j\omega\mu_0(\sigma_\mathrm{g} + j\omega(\varepsilon_\mathrm{r}-1)\varepsilon_0)}\right)}\cos(r_\mathrm{ij}\lambda)d\lambda, \tag{7}$$

where μ_0 is the vacuum magnetic permeability μ_0 = $4\pi \times 10^{-7}$ H/m, h_i and h_j [m] are the conductor's height above the soil, σ_g [S/m] is the soil conductivity, ε_r is the relative permittivity, ε_0 is the vacuum permittivity (ε_0 = 8.854 $\times 10^{-12}$ F/m), μ_g is the magnetic permeability of the soil (in practical applications is assumed to be equal to the vacuum magnetic permeability) and r_ij [m] is the horizontal distance between the conductors. The γ_g^2 and γ_0^2 are the squared propagation constants of the air and soil ($\gamma_\mathrm{g}^2 = j\omega\mu_\mathrm{g}(j\omega\varepsilon_\mathrm{r}\varepsilon_0 + \sigma_\mathrm{g})$ and $\gamma_0^2 = -\omega^2\mu_0\varepsilon_0$), respectively. The integration variable λ represents the spatial frequency of the Fourier spectrum which is related to the energy attenuation throughout the soil layer (or layers in a stratified soil) [31].

The frequency dependence of soils can be inserted in the Nagakawa approach, where the $\sigma_\mathrm{g} \rightarrow \sigma_\mathrm{g}(f)$ and $\varepsilon_\mathrm{r} \rightarrow \varepsilon_\mathrm{r}(f)$ are substituted for each formulation proposed. In the next section, four causal formulations of FD soil electrical parameters are presented.

4. Modeling of Soil for Fast-Front Transients

Accurate computation of the transient responses on power systems depends on adequate modeling of the ground and on the type of disturbance. In this context, when a phenomenon of low-frequency content is involved, the soil can be represented by a constant resistivity (ρ_g = $1/\sigma_\mathrm{g}$) [36]. However, when fast-front phenomena such as lightning strikes, characterized for high-frequency content varying from dc up to few MHz, are involved, the variation of resistivity and permittivity of soils with the frequency must be taken into account in the simulations [37]. FD ground can be characterized by the soil resistivity ($\rho_\mathrm{g}(f)$ = $1/\sigma_\mathrm{g}(f)$), relative permittivity $\varepsilon_\mathrm{r}(f)$ [21,38]. However, in practical engineering cases, the magnetic permeability is considered equal to the vacuum ($\mu \approx \mu_0$). Several approaches for FD soils are presented in the literature as summarized in [13,22] where distinct formulations based on several laboratory and/or field measurement have been carried out. We briefly present the equations concerning the frequency dependence of the soil parameters and some causal approaches proposed in the literature.

4.1. Frequency-Dependent Soil Modeling

Soils are composed of a complex formation of compacted layers of earth with organic and inorganic materials disintegrated. Besides the frequency, the soil electrical parameters depends on environmental factors such as the temperature, humidity and particles [30]. From the electromagnetism, the Ampère-Maxwell's equation relates the magnetic field intensity $\vec{H}$ [A/m] to the electric conductive current density $\vec{J}_\mathrm{c} = \sigma_\mathrm{g}\vec{E}$ [A/m^2] and the displacement current density $\vec{J_{\rm D}}$ [A/m^2] in a dielectric medium when an external electrical field $\vec{E}$ [V/m] is applied, as follows [36,37]

$$\nabla \times \vec{H} = \vec{J_{\rm c}} + \vec{J_{\rm D}} = \sigma_0 \vec{E} + j\omega\varepsilon_{\rm r}\vec{E}, \tag{8}$$

where σ_0 [S/m] is the conductivity at low frequency (LF), considered as a real number associated with the transport of electric charge and losses generated during the conducting process. However, the relative permittivity ($\varepsilon_{\rm r}$) is a complex number which can be written as

$$\varepsilon_{\rm r} = \varepsilon_{\rm r}' - j\varepsilon_{\rm r}'', \tag{9}$$

where $\varepsilon_{\rm r}'$ is related to the ability of the material to be polarized and store energy whereas $\varepsilon_{\rm r}''$ represents the losses due to the heat generated by the dipole frictions in the several polarization processes as detailed in [36,37]. Combining (9) into (8), yields

$$\nabla \times \vec{H} = \left[\left(\sigma_0 + \omega\varepsilon_{\rm r}''\right) + j\omega\varepsilon_{\rm r}'\right]\vec{E} = \left(\sigma_{\rm eff} + j\omega\varepsilon_{\rm r}'\right)\vec{E}. \tag{10}$$

The effective conductivity $\sigma_{\rm eff}$ [S/m] increases with the frequency whereas the $\varepsilon_{\rm r}'$ decreases as the frequency of the applied field increases as detailed in [36]. The explanation related to the electric resistivity $\rho_{\rm g}$ and relative permittivity $\varepsilon_{\rm r}$, and the different polarization processes in the ground molecules are given in [39]. As the frequency increases, the polarization processes are not able to follow the fast alternations of the electric field $\vec{E}$. As a consequence, the $\varepsilon_{\rm r}'$ decreases with the increasing frequency. However, at high frequencies, the $\varepsilon_{\rm r}''$ representing the losses per cycle increases. As a result, the $\sigma_{\rm eff}$ increases while the value of $\varepsilon_{\rm eff}$ decreases for the increasing frequency.

4.2. Closed-Form Expressions for the Soil Approaches

In this section, we consider only causal models with their respective expressions proposed to represent FD soil electrical parameters (resistivity and relative permittivity). They are: Longmire-Smith (LS), Messier (M) and Portela (P) where the causality of these models were proved using the Kramers–Kronig relationships as detailed in [22]. Additionally, the causality of Alípio-Visacro (AV) model has been proved in [21,23,36]. These four FD soil models are described as follows:

4.2.1. Longmire-Smith (LS) Expressions

Longmire et al. developed an analytical representation for the FD soil parameters in the 1970s [40,41]. These formulae were based on the Scott's [42] and Wilkenfeld's experimental data. The proposed FD conductivity $\sigma_{\rm g}(f)$ and FD relative permittivity $\varepsilon_{\rm r}(f)$ are given by

$$\sigma_{\rm g}(f) = \sigma_0 + 2\pi\varepsilon_0 \sum_{i=1}^{13} a_{\rm i} F_{\rm i} \frac{(f/F_{\rm i})^2}{1 + (f/F_{\rm i})^2}, \tag{11}$$

$$\varepsilon_{\rm r}(f) = \varepsilon_\infty + \sum_{i=1}^{13} \frac{a_{\rm i}}{1 + (f/F_{\rm i})^2}, \tag{12}$$

$$F_{\rm i} = (125\sigma_0)^{0.8312} \times 10^{i-1}, \tag{13}$$

where the coefficients $a_{\rm i}$'s are specified in the Table I of [41] and ε_∞ is the high frequency limit of the permeability and is set to 5. The expressions are valid in the frequency range of 1 Hz to 10^{12} Hz.

4.2.2. Messier (M) Expressions

The expressions proposed by Messier [43,44] for the $\sigma_g(f)$ and $\varepsilon_r(f)$ as a function of frequency are also based on Scott's data [42] being valid for the frequency range of 100 Hz to 1 MHz. These expressions are written as [13]

$$\sigma_g(f) = \sigma_0 + \sqrt{4\pi f \sigma_0 \varepsilon_0 \varepsilon_\infty}, \tag{14}$$

$$\varepsilon_r(f) = \varepsilon_\infty + \sqrt{\frac{1}{\pi}\frac{\sigma_0 \varepsilon_\infty}{f \varepsilon_0}}, \tag{15}$$

where ε_∞ is set to 8.

4.2.3. Portela (P) Expressions

Portela performed a large number of measurements obtained in different areas in Brazil in the frequency range of 100 Hz to 2 MHz [38]. The FD $\sigma_g(f)$ and FD $\varepsilon_r(f)$ are expressed by

$$\sigma_g(f) = \sigma_0 + \Delta_i \left[\cot\left(\frac{\pi}{2}\alpha'\right)\right]\left(\frac{f}{10^6}\right)^{\alpha'}, \tag{16}$$

$$\varepsilon_r(f) = \Delta_i \left(\frac{f}{10^6}\right)^{\alpha'} \frac{1}{2\pi f \varepsilon_0}, \tag{17}$$

where α' is an adjustable parameter of soil, $\Delta_i = 2\pi f \varepsilon$ is computed at 1 MHz, which also depends on the soil model. In this study, the median values $\alpha = 0.706$ and $\Delta_i = 11.71$ mS/m were considered based on [24].

4.2.4. Alípio-Visacro (AV) Expressions

Based on a large number of field measurements in different locations in Brazil, Alípio-Visacro have proposed the curve-fit expression to compute the FD $\sigma_g(f)$ and FD $\varepsilon_r(f)$, given by [21]

$$\sigma_g(f) = \sigma_0 + \sigma_0 \times h(\sigma_0)\left(\frac{f}{1 \times 10^6}\right)^{\xi}, \tag{18}$$

$$\varepsilon_r(f) = \frac{\varepsilon_{\infty'}}{\varepsilon_0} + \frac{\tan(\pi\xi/2) \times 10^{-3}}{2\pi\varepsilon_0 (1 \times 10^6)^{\xi}} \sigma_0 \times h(\sigma_0) f^{\xi - 1}, \tag{19}$$

$$h(\sigma_0) = 1.26\sigma_0^{-0.73}, \tag{20}$$

where $\varepsilon_{\infty'}/\varepsilon_0$ and ξ are set to 12 and 0.54, respectively, based on [21]. The expressions are valid in the frequency range of 100 Hz to 4 MHz.

To investigate the behaviour of the four soil models, a comparison is carried out for the FD soil resistivity ($\rho_g(f) = 1/\sigma_g(f)$) and relative permittivity in the frequency range of 100 Hz to 10 MHz. Following the recommendations in the CIGRÈ WG C4.33 brochure [23] depicted in Table 5.1 for transmission line analysis, two low-frequency (100 Hz) resistivities ($\rho_0 = 1/\sigma_0$) of 700 and 4000 Ω·m are adopted. For the frequency-constant soil, labeled as 'C', soils of 700 and 4000 Ω·m and relative permittivity ε_r of 10 are assumed. The comparisons are illustrated in Figures 1 and 2.

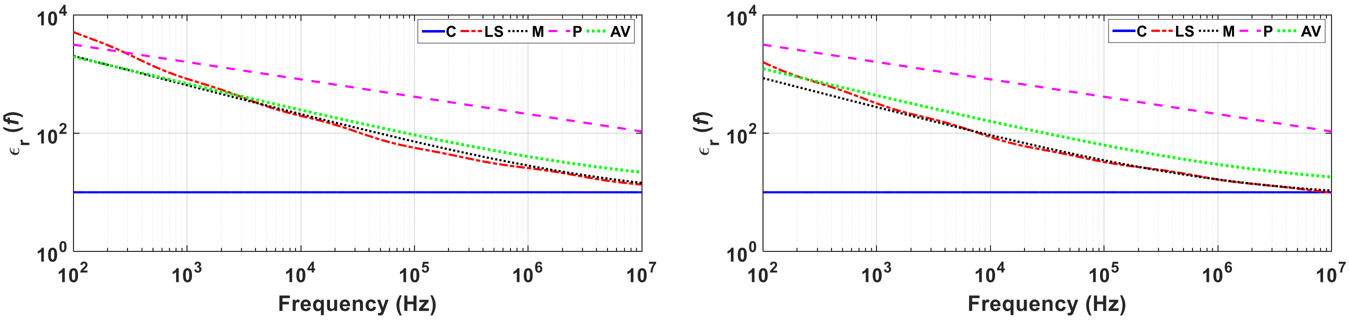

(**a**) (**b**)

Figure 1. Relativity permittivity as a function of frequency with ρ_0 of: (**a**) 700 Ω·m and (**b**) 4000 Ω·m.

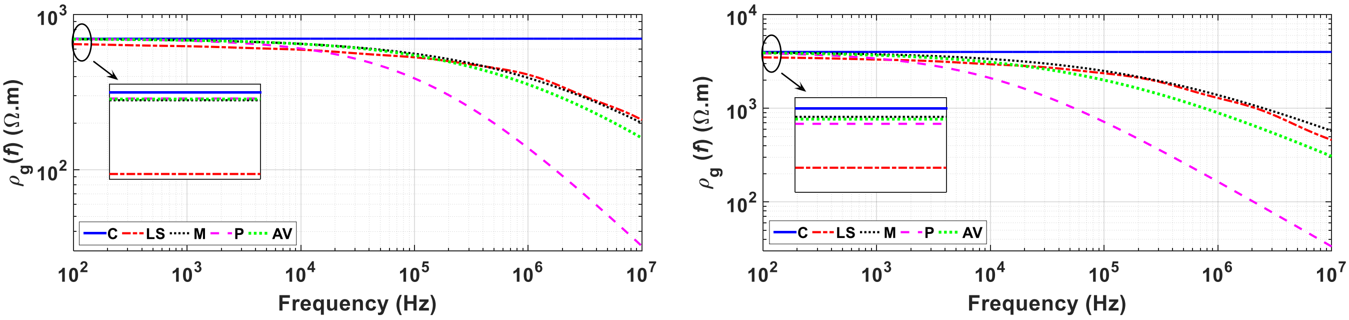

(**a**) (**b**)

Figure 2. Soil resistivity as a function of frequency with ρ_0 of: (**a**) 700 Ω·m and (**b**) 4000 Ω·m.

It can be seen that FD soil resistivity and relative permittivity decrease significantly as frequency increases, especially for the high-resistive soil. The FD relative permittivity is much larger at low frequencies than those computed at high frequencies, which tends to usual values employed in grounding studies. In Figure 2, at low frequencies, the Longmire-Smith (LS) model presented the lower value of resistivity. However, as the frequency increases, one notes that the FD soil resistivity calculated by the Portela (P) model showed a much higher difference in comparison with those calculated for the other FD soil models [13,22]. In order to quantify this difference, the percentage variation of the resistivity $(\Delta\rho)\%$ is calculated as follows

$$\Delta\rho(\%) = \left|\frac{\rho(10\ \text{MHz}) - \rho(100\ \text{Hz})}{\rho(100\ \text{Hz})}\right| \times 100\%, \tag{21}$$

where $\rho(100\ \text{Hz})$ is the low-frequency resistivity calculated at 100 Hz and $\rho(10\ \text{MHz})$ is measured at 10 MHz. The calculated $(\Delta\rho)\%$ for both soils are shown in Tables 2 and 3.

Table 2. $\Delta\rho(\%)$ for the FD soil models considering the soil of ρ_0 of 700 Ω.m.

FD Soil Model	ρ(100 Hz)	ρ(10 MHz)	$\Delta\rho(\%)$
LS	645.4	209.6	67.52
M	694.5	200.3	71.15
P	695.7	32.21	95.37
AV	695.3	160.3	76.94

Table 3. $\Delta\rho(\%)$ for the FD soil models considering the soil of ρ_0 of 4000 Ω.m.

FD Soil Model	ρ(100 Hz)	ρ(10 MHz)	$\Delta\rho(\%)$
LS	3500	459.4	86.87
M	3926	574.3	85.37
P	3865	33.48	99.13
AV	3906	307.2	92.13

As seen in these tables, the Longmire-Smith (LS) model has presented the lowest values of ρ_0 for both type of soils. However, the Portela (P) model has shown the highest $\Delta\rho(\%)$ among the all FD others, where this $\Delta\rho(\%)$ is higher as the soil resistivity increases. According to CIGRÈ WG C4.33 [23], the Portela (P) model suffers from the lack of reliability in its experiments to determine the parameters α' and Δ_i in (16) and (17). As a result, Portela's (P) model deviates significantly from Longmire-Smith (LS), Messier (M) and Alípio-Visacro (AV) models, which predict a more pronounced variation of the resistivity and relative permittivity as illustrated in Figures 1 and 2. As a consequence, the Portela (P) model will cause significant impact on the ground-return parameters and on the transient response voltages. Besides that, it is noted that the curves for Longmire-Smith (LS), Messier (M) and Alípio-Visacro (AV) models tend to present similar values, especially for the low-resistive soil. As the frequency increases, the difference between these FD soils become significant for a high-resistive soil [23]. As a result, it is expected that the transience generated by fast-front phenomena on OHTLs located on poorly conducting soil will have an expressive impact on the transient responses, as further illustrated.

5. Modal Decoupling of an OHTL

An OHTL of n conductors (phase conductors and ground wires) of length ℓ [km] can be generically represented as illustrated in Figure 3. In the frequency domain, the voltage $\boldsymbol{V}$ and current $\boldsymbol{I}$ are related to the sending (A) and receiving (B) ends, as follows [45]

$$\frac{\partial \boldsymbol{V}(\omega)}{\partial x} = -\boldsymbol{Z}_{\boldsymbol{\ell}}(\omega)\ \boldsymbol{I}(\omega), \tag{22}$$

$$\frac{\partial \boldsymbol{I}(\omega)}{\partial x} = -\boldsymbol{Y}_{\mathrm{t}}(\omega)\ \boldsymbol{V}(\omega), \tag{23}$$

where x [km] is the horizontal distance from the sending end. $\boldsymbol{Z}_{\boldsymbol{\ell}}(\omega)$ and $\boldsymbol{Y}_{\mathrm{t}}(\omega)$ are $n \times n$ matrices whereas $\boldsymbol{V}(\omega)$ and $\boldsymbol{I}(\omega)$ are vectors of length $n \times 1$. By differentiating (22) and (23) replacing the first derivatives back into the second derivatives, it yields [45]

$$\frac{\partial^2 \boldsymbol{V}(\omega)}{\partial x^2} = \boldsymbol{Z}_{\boldsymbol{\ell}}(\omega)\boldsymbol{Y}_{\mathrm{t}}(\omega)\ \boldsymbol{V}(\omega) = \boldsymbol{S}_{\mathrm{V}}(\omega)\boldsymbol{V}(\omega), \tag{24}$$

$$\frac{\partial^2 \boldsymbol{I}(\omega)}{\partial x^2} = \boldsymbol{Y}_{\mathrm{t}}(\omega)\boldsymbol{Z}_{\boldsymbol{\ell}}(\omega)\ \boldsymbol{I}(\omega) = \boldsymbol{S}_{\mathrm{I}}(\omega)\boldsymbol{I}(\omega), \tag{25}$$

where $\boldsymbol{S}_{\mathrm{V}}(\omega)$=$\boldsymbol{Z}_{\boldsymbol{\ell}}(\omega)\boldsymbol{Y}_{\mathrm{t}}(\omega)$ and $\boldsymbol{S}_{\mathrm{I}}(\omega)$=$\boldsymbol{Y}_{\mathrm{t}}(\omega)\boldsymbol{Z}_{\boldsymbol{\ell}}(\omega)$ where the $\boldsymbol{S}_{\mathrm{V}}(\omega)$ and $\boldsymbol{S}_{\mathrm{I}}(\omega)$ are symmetrical matrices. Then the following relationship is valid

$$\boldsymbol{S}_{\mathrm{V}}(\omega) = \boldsymbol{S}_{\mathrm{I}}^{\mathrm{T}}(\omega). \tag{26}$$

Due to conditions in (26), $\boldsymbol{S}_{\mathrm{V}}(\omega)$ and $\boldsymbol{S}_{\mathrm{I}}(\omega)$ present the same polynomial characteristic and same eigenvalues $\boldsymbol{\lambda}(\omega)$, however they do not have the same eigenvectors [9]. Thus, the matrix with eigenvalues $\boldsymbol{\lambda}(\omega)$ is related to $\boldsymbol{S}_{\mathrm{V}}(\omega)$ and $\boldsymbol{S}_{\mathrm{I}}(\omega)$ through the eigenvectors $\boldsymbol{T}_{\mathrm{V}}(\omega)$ and $\boldsymbol{T}_{\mathrm{I}}(\omega)$ [9,46]

$$\boldsymbol{\lambda}(\omega) = \boldsymbol{T}_{\mathrm{V}}^{-\mathbf{1}}(\omega)\boldsymbol{S}_{\mathrm{V}}(\omega)\boldsymbol{T}_{\mathrm{V}}(\omega) = \boldsymbol{T}_{\mathrm{V}}^{-\mathbf{1}}(\omega)\boldsymbol{Z}_{\boldsymbol{\ell}}(\omega)\boldsymbol{Y}_{\boldsymbol{t}}(\omega)\boldsymbol{T}_{\mathrm{V}}(\omega), \tag{27}$$

$$\boldsymbol{\lambda}(\omega) = \boldsymbol{T}_{\mathrm{I}}^{-1}(\omega)\boldsymbol{S}_{\mathrm{I}}(\omega)\boldsymbol{T}_{\mathrm{I}}(\omega) = \boldsymbol{T}_{\mathrm{I}}^{-1}(\omega)\boldsymbol{Y}_{t}(\omega)\boldsymbol{Z}_{\ell}(\omega)\boldsymbol{T}_{\mathrm{I}}(\omega). \tag{28}$$

The $\boldsymbol{T}_{\mathrm{V}}(\omega)$ and $\boldsymbol{T}_{\mathrm{I}}(\omega)$ are named *transformation matrices* which are frequency dependent due to the fact $\boldsymbol{Z}_{\ell}(\omega)$ and $\boldsymbol{Y}_{\mathrm{t}}(\omega)$ vary with frequency. Furthermore, these transformation matrices follow the relationship [9]

$$\boldsymbol{T}_{\mathrm{V}}^{-1}(\omega) = \boldsymbol{T}_{\mathrm{I}}^{\mathrm{T}}(\omega). \tag{29}$$

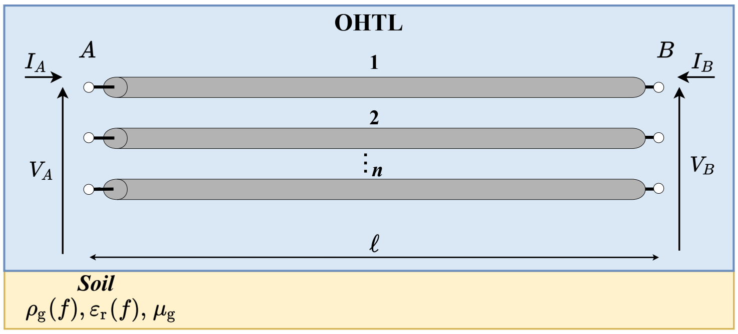

Figure 3. Multiphase OHTL of length ℓ.

Isolating the products $\boldsymbol{Z}_{\ell}(\omega)\boldsymbol{Y}_{\mathrm{t}}(\omega)$ in (27) and $\boldsymbol{Y}_{\mathrm{t}}(\omega)\boldsymbol{Z}_{\ell}(\omega)$ in (28), it yields

$$\boldsymbol{Z}_{\ell}(\omega)\boldsymbol{Y}_{\mathrm{t}}(\omega) = \boldsymbol{T}_{\mathrm{V}}(\omega)\boldsymbol{\lambda}(\omega)\boldsymbol{T}_{\mathrm{V}}^{-1}(\omega), \tag{30}$$

$$\boldsymbol{Y}_{\mathrm{t}}(\omega)\boldsymbol{Z}_{\ell}(\omega) = \boldsymbol{T}_{\mathrm{I}}(\omega)\boldsymbol{\lambda}(\omega)\boldsymbol{T}_{\mathrm{I}}^{-1}(\omega). \tag{31}$$

Replacing the (30) in (24) and (31) in (25), the expressions are rewritten as following

$$\frac{\partial^2}{\partial x^2}\left[\boldsymbol{T}_{\mathrm{V}}^{-1}(\omega)\boldsymbol{V}(\omega)\right] = \boldsymbol{\lambda}(\omega)\boldsymbol{T}_{\mathrm{V}}^{-1}(\omega)\boldsymbol{V}(\omega) \Rightarrow \frac{\partial^2}{\partial x^2}\boldsymbol{V}_{\mathrm{m}}(\omega) = \boldsymbol{\lambda}(\omega)\boldsymbol{V}_{\mathrm{m}}(\omega), \tag{32}$$

$$\frac{\partial^2}{\partial x^2}\left[\boldsymbol{T}_{\mathrm{I}}^{-1}(\omega)\boldsymbol{I}(\omega)\right] = \boldsymbol{\lambda}(\omega)\boldsymbol{T}_{\mathrm{I}}^{-1}(\omega)\boldsymbol{I}(\omega) \Rightarrow \frac{\partial^2}{\partial x^2}\boldsymbol{I}_{\mathrm{m}}(\omega) = \boldsymbol{\lambda}(\omega)\boldsymbol{I}_{\mathrm{m}}(\omega). \tag{33}$$

Based on (32) and (33), the voltages and currents are in the modal domain (m) which can be expressed as

$$\boldsymbol{V}_{\mathrm{m}}(\omega) = \boldsymbol{T}_{\mathrm{V}}^{-1}(\omega)\boldsymbol{V}(\omega) \Rightarrow \boldsymbol{V}(\omega) = \boldsymbol{T}_{\mathrm{V}}(\omega)\boldsymbol{V}_{\mathrm{m}}(\omega), \tag{34}$$

$$\boldsymbol{I}_{\mathrm{m}}(\omega) = \boldsymbol{T}_{\mathrm{I}}^{-1}(\omega)\boldsymbol{I}(\omega) \Rightarrow \boldsymbol{I}(\omega) = \boldsymbol{T}_{\mathrm{I}}(\omega)\boldsymbol{I}_{\mathrm{m}}(\omega). \tag{35}$$

Using the relations (34) and (35) in the (22) and (23), yields [9]

$$\frac{\partial}{\partial x}\boldsymbol{V}_{\mathrm{m}}(\omega) = -\boldsymbol{T}_{\mathrm{V}}^{-1}(\omega)\boldsymbol{Z}_{\ell}(\omega)\boldsymbol{T}_{\mathrm{I}}(\omega)\boldsymbol{I}_{\mathrm{m}}(\omega) = -\boldsymbol{Z}_{\mathrm{m}}(\omega)\boldsymbol{I}_{\mathrm{m}}(\omega), \tag{36}$$

$$\frac{\partial}{\partial x}\boldsymbol{I}_{\mathrm{m}}(\omega) = -\boldsymbol{T}_{\mathrm{I}}^{-1}(\omega)\boldsymbol{Y}_{t}(\omega)\boldsymbol{T}_{\mathrm{V}}(\omega)\boldsymbol{V}_{\mathrm{m}}(\omega) = -\boldsymbol{Y}_{\mathrm{m}}(\omega)\boldsymbol{V}_{\mathrm{m}}(\omega), \tag{37}$$

where modal impedance matrix $\boldsymbol{Z}_{\mathrm{m}}(\omega)$ and modal admittance matrix $\boldsymbol{Y}_{\mathrm{m}}(\omega)$ are defined as [9,46]

$$\boldsymbol{Z}_{\mathrm{m}}(\omega) = \boldsymbol{T}_{\mathrm{V}}^{-1}(\omega)\boldsymbol{Z}_{\ell}(\omega)\boldsymbol{T}_{\mathrm{I}}(\omega), \tag{38}$$

$$\boldsymbol{Y}_{\mathrm{m}}(\omega) = \boldsymbol{T}_{\mathrm{I}}^{-1}(\omega)\boldsymbol{Y}_{\mathrm{t}}(\omega)\boldsymbol{T}_{\mathrm{V}}(\omega). \tag{39}$$

There are several algorithms proposed in the literature to calculate the eigenvalues and eigenvectors in the modal FD transformation matrices such as the Newton-Raphson [46], Schur-Cholesky [9], sequential quadratic programming [3] and Levenberg–Marquardt [47] algorithms. However, when certain conditions on the tower symmetry are satisfied, a real and constant transformation matrix, the so-called Clarke's matrix, can be used as $\boldsymbol{T}_{\mathrm{I}} = \boldsymbol{T}_{\mathrm{Clarke}}$, as detailed in [9,48].

An OHTL of n-phases can be decoupled into n propagation modes that can be interpreted as independent single-phase transmission lines in the modal domain [9]. In this work a three-phase transmission line is decoupled into three single-phase lines where the modes m are defined here as MODE α, MODE β and MODE 0, as depicted in Figure 4.

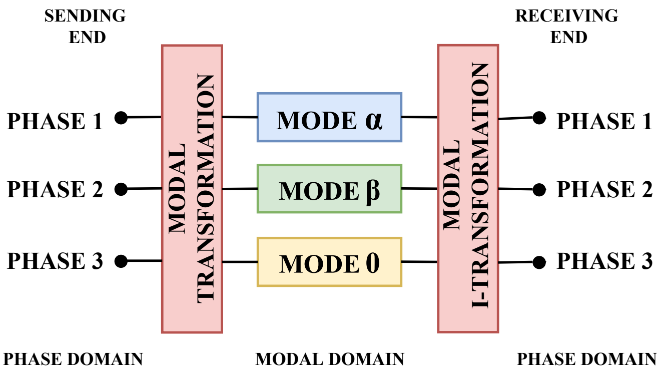

Figure 4. Modal- and phase-domain representations for modeling a three-phase OHTL.

The frequency-domain equations related to each single-phase line in the modal domain m can be expressed as follows [9]

$$\begin{bmatrix} V_{\mathrm{m}}^{\mathrm{A}}(\omega) \\ I_{\mathrm{m}}^{\mathrm{A}}(\omega) \end{bmatrix} = \begin{bmatrix} \cosh(\gamma_{\mathrm{m}}(\omega)\ell) & Z_{\mathrm{m}}^{\mathrm{C}}(\omega)\sinh(\gamma_{\mathrm{m}}(\omega)\ell) \\ 1/Z_{\mathrm{m}}^{\mathrm{C}}(\omega)\sinh(\gamma_{\mathrm{m}}(\omega)\ell) & \cosh(\gamma_{\mathrm{m}}(\omega)\ell) \end{bmatrix} \begin{bmatrix} V_{\mathrm{m}}^{\mathrm{B}}(\omega) \\ I_{\mathrm{m}}^{\mathrm{B}}(\omega) \end{bmatrix}, \tag{40}$$

where A is the sending end and B is the receiving end, $V(\omega)$ and $I(\omega)$ are the respective voltage and currents for a certain mode m and ℓ is the line length. The modal propagation function $\gamma_{\mathrm{m}}(\omega)$ and the impedance characteristic $Z_{\mathrm{m}}^{\mathrm{C}}(\omega)$ are given by [9]

$$\gamma_{\mathrm{m}}(\omega) = \sqrt{Z_{\mathrm{m}}(\omega)Y_{\mathrm{m}}(\omega)}, \tag{41}$$

$$Z_{\mathrm{m}}^{\mathrm{C}}(\omega) = \sqrt{Z_{\mathrm{m}}(\omega)/Y_{\mathrm{m}}(\omega)}. \tag{42}$$

The attenuation constant $\lambda_{\mathrm{m}}(\omega)$ [km^{-1}] and the propagation velocity $\mathrm{v}_{\mathrm{m}}(\omega)$ [km/s] can be calculated as follows

$$\lambda_{\mathrm{m}}(\omega) = \Re\{\gamma_{\mathrm{m}}(\omega)\}, \tag{43}$$

$$\mathrm{v}_{\mathrm{m}}(\omega) = \frac{\omega}{\Im\{\gamma_{\mathrm{m}}(\omega)\}}, \tag{44}$$

where $\Re$ and $\Im$ are the real and imaginary parts of the number $\gamma_{\mathrm{m}}(\omega)$. The propagation modes (m) are labeled here as α, β and 0. Assuming that $I_{\mathrm{m}}^{B}(\omega) = 0$, each frequency-domain modal voltage at the sending and receiving ends for the open-circuit OHTL of length ℓ can be computed as follows

$$V_{\mathrm{m}}^{\mathrm{A}}(\omega) = [\cosh(\gamma_{\mathrm{m}}(\omega)\ell)]\, V_{\mathrm{m}}^{\mathrm{B}}(\omega), \tag{45}$$

$$V_{\mathrm{m}}^{\mathrm{B}}(\omega) = Z_{\mathrm{m}}^{\mathrm{C}}(\omega)\sinh^{-1}(\gamma_{\mathrm{m}}(\omega)\ell) I_{\mathrm{m}}^{\mathrm{A}}(\omega), \tag{46}$$

where $V_{\mathrm{m}}(\omega)$ and $I_{\mathrm{m}}(\omega)$ are the modal-domain voltages developed and injected currents at the sending (A) and receiving (B) ends of the line. Once the modal voltages $V_{\mathrm{m}}(\omega)$ are calculated for the whole frequency range, the phase-domain voltages in the phases 1, 2 and $3 - \boldsymbol{V}_{123}(\omega)$ are calculated as follows [9]

$$\boldsymbol{V}_{123}^{\mathrm{B}}(\omega) = \boldsymbol{T}_{\mathrm{V}}(\omega)\boldsymbol{V}_{\mathrm{m}}^{\mathrm{B}}(\omega), \tag{47}$$

where $\boldsymbol{V}_{123}^{\mathrm{B}}(\omega) = [V_1^B \quad V_2^B \quad V_3^B]^{\mathrm{T}}$ and $\boldsymbol{V}_{\mathrm{m}}^{B}(\omega) = [V_\alpha^B \quad V_\beta^B \quad V_0^B]^{\mathrm{T}}$. The FD voltages $\boldsymbol{V}_{123}(\omega)$ are converted from frequency to time domain using the Numerical Inverse Laplace Transform (NILT) method as described in [49].

The steps summarizing all the procedure adopted in this work to compute the voltages and currents on a three-phase OHTL using the modal decomposition are illustrated in Figure 5.

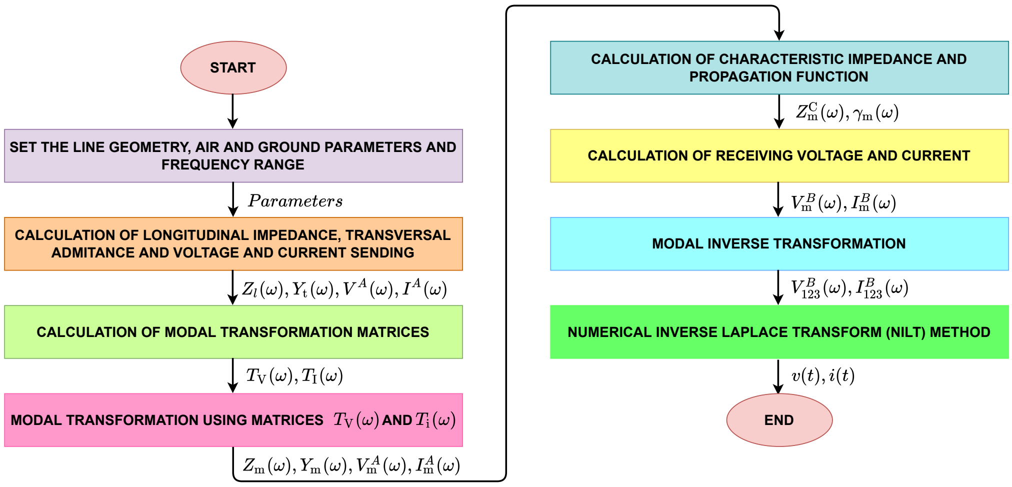

Figure 5. Flow-chart with the the voltages and currents on a three-phase OHTL using the modal decomposition model.

6. Ground Wires

In general, the OHTL is composed of n_{f} phase conductors and equipped with n_{g} overhead ground wire conductors located at the top of the tower structure. Ground wires must protect the phase conductors intercepting lightning strokes, conduct part of the fault current and mitigate the dangerous voltages generated [50]. Considering that (1) and (2) represent a multiphase OHTL of n phases (being $n = n_{\mathrm{f}} + n_{\mathrm{g}}$), the longitudinal impedance matrix $\boldsymbol{Z}_\ell(\omega)$ and transversal admittance matrix $\boldsymbol{Y}_{\mathrm{t}}(\omega)$, both of dimension $n \times n$, can be reorganized as follows [51–53]

$$\boldsymbol{Z}_\ell(\omega) = \begin{bmatrix} \boldsymbol{Z}_{\mathrm{uu}} & \boldsymbol{Z}_{\mathrm{ug}} \\ \boldsymbol{Z}_{\mathrm{ug}}^T & \boldsymbol{Z}_{\mathrm{gg}} \end{bmatrix}, \tag{48}$$

$$\boldsymbol{Y}_{\mathrm{t}}(\omega) = \begin{bmatrix} \boldsymbol{Y}_{\mathrm{uu}} & \boldsymbol{Y}_{\mathrm{ug}} \\ \boldsymbol{Y}_{\mathrm{ug}}^{\mathrm{T}} & \boldsymbol{Y}_{\mathrm{gg}} \end{bmatrix} = j\omega \begin{bmatrix} \boldsymbol{C}_{\mathrm{uu}} & \boldsymbol{C}_{\mathrm{ug}} \\ \boldsymbol{C}_{\mathrm{ug}}^{\mathrm{T}} & \boldsymbol{C}_{\mathrm{gg}} \end{bmatrix} = j\omega \begin{bmatrix} \boldsymbol{E}_{\mathrm{uu}} & \boldsymbol{E}_{\mathrm{ug}} \\ \boldsymbol{E}_{\mathrm{ug}}^{\mathrm{T}} & \boldsymbol{E}_{\mathrm{gg}} \end{bmatrix}^{-1}, \tag{49}$$

where the index $_{\mathrm{uu}}$ represents the system without the set of ground wires (grounded-less), the index $_{\mathrm{ug}}$ represents the grounded-less system with the ground wires, and the index $_{\mathrm{gg}}$ represents the set of ground wires only and $\boldsymbol{E}$ [V/km] is the electric field [52]. In most of the practical cases, the ground wires are continuously grounded in each tower structure, in which the voltage drop between two ground wires can be approximately zero [52,53]. In this case, the current at the ground wires I_{gg} is equal to zero, then the (48) and (49), based on the Kron's reduction, can be rewritten as [51–53]

$$\boldsymbol{Z}_\ell'(\omega) = \boldsymbol{Z}_{\mathrm{uu}} - \boldsymbol{Z}_{\mathrm{ug}}\boldsymbol{Z}_{\mathrm{gg}}^{-1}\boldsymbol{Z}_{\mathrm{ug}}^{\mathrm{T}}, \tag{50}$$

$$\boldsymbol{Y}_{\mathrm{t}}'(\omega) = j\omega[\boldsymbol{E}_{\mathrm{uu}} - \boldsymbol{E}_{\mathrm{ug}}\boldsymbol{E}_{\mathrm{gg}}^{-1}\boldsymbol{E}_{\mathrm{ug}}^{\mathrm{T}}]^{-1}. \tag{51}$$

In (50) and (51), $\boldsymbol{Z}_\ell'(\omega)$ and $\boldsymbol{Y}_{\mathrm{t}}'(\omega)$ are the longitudinal impedance and the transversal admittance matrices in their reduced forms without the ground wires, respectively. This representation takes into account the effects of the ground wires on the phase conductors and the resulting OHTL has only n_{f} equivalent phase conductors without ground wires [51,53]. After that, modal decomposition can be applied into the $\boldsymbol{Z}'_\ell$ and $\boldsymbol{Y}'_\mathrm{t}$ to study the electromagnetic transients.

7. Numerical Results and Discussions

In order to investigate the influence of the FD soil models on the voltages developed by a lightning strike on 440-kV OHTL, simulations concerning modal- and phase-domains were carried out for the analysis. For this purpose, a three-phase OHTL with ground wires and two distinct lengths (ℓ) of 1 km and 10 km located on FD ground were considered in these simulations. The configuration of the studied OHTL is illustrated in Figure 6. The four FD soi models, Longmire-Smith (LS), Messier (M), Portela (P) and Alípio-Visacro (AV), previously presented are taken into account. Two values of low-frequency resistance ρ_0 of 700 and 4000 $\Omega{\cdot}$m are assumed. Then, the FD resistivity $\rho_\mathrm{g}(f)$ and $\varepsilon_\mathrm{r}(f)$ from (11) to (20) are employed.

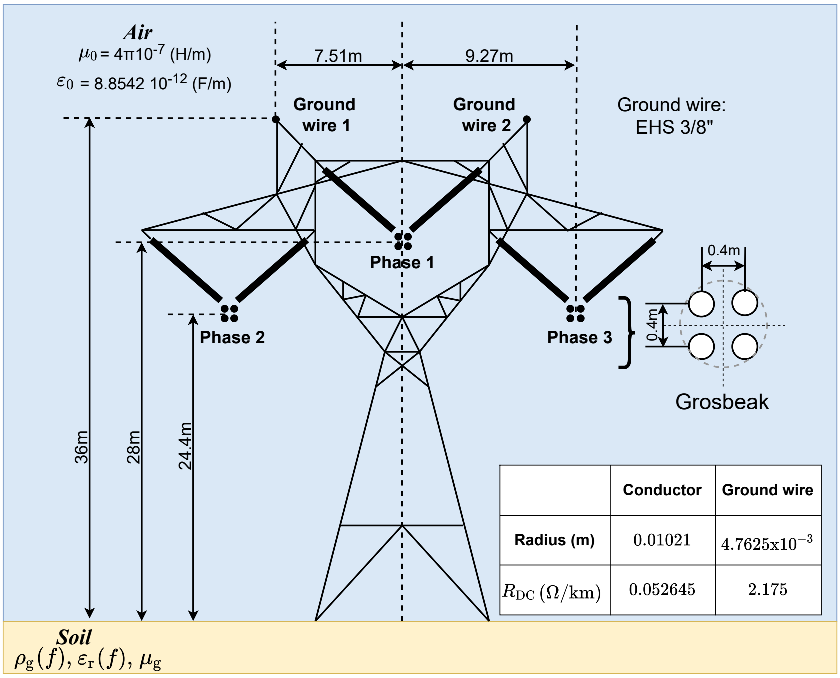

Figure 6. Configuration of the 440-kV OHTL with vertical symmetry studied.

For this analysis, the tower surge impedance and the soil ionization effects were neglected. The Nagakawa's formulations, modal transformation algorithms and simulations were developed in MATLAB programming language. It is worth mentioning that four FD soil models employed in this work have been determined under distinct frequency ranges. However, both relative permittivity and resistivity present a monotone behavior for the increasing frequency. Due to a causal relationship between these electric parameters, there is guaranteed asymptotic behavior which can be extended to 10 MHz [2,22].

7.1. Influence of the FD Soil Models on Impedance and on Admittance

Firstly, the impact of the FD soil models on the elements of the ground-return impedance matrix $\boldsymbol{Z}_\mathrm{g}(\omega)$ and ground-return admittance matrix $\boldsymbol{Y}_\mathrm{g}(\omega)$ are computed for the four approaches presented. In this analysis, two values of the low-frequency resistivities (ρ_0) of 700 and 4000 $\Omega{\cdot}$m are considered for the FD soil models, in which the σ_g and ε_r are calculated by LS in (11) and (12), M in (14) and (15), P in (16) and (17), AV in (18) and (19). The results are compared with those obtained for the frequency-constant soil model (C), assuming soils of 700 and 4000 $\Omega{\cdot}$m and relative permittivity ε_r of 10. The ground-return impedance is calculated as shown in (3) and (4) while the ground-return admittance is calculated as shown in (5)–(7). The OHTL is a symmetrical line with two ground wires as depicted in

Figure 6, resulting into $\mathbf{Z}_\mathrm{g}(\omega)$ and $\mathbf{Y}_\mathrm{g}(\omega)$ of dimensions 5×5. We have chosen to plot the elements $Z_{\mathrm{g}11}$, $Z_{\mathrm{g}12}$, $Z_{\mathrm{g}14}$ and $Z_{\mathrm{g}44}$ and the elements $Y_{\mathrm{g}11}$, $Y_{\mathrm{g}12}$, $Y_{\mathrm{g}14}$ and $Y_{\mathrm{g}44}$, as (1,1) represents a proper element for the phase conductor 1, (1,2) represents a mutual element between phase conductors, (1,4) represents mutual element between phase and ground wires conductors and (4,4) represents a proper element for the ground wire 4.

The ground-return impedance elements are depicted in Figure 7 for soils of 700 Ω·m (on the left) and 4000 Ω·m (on the right).

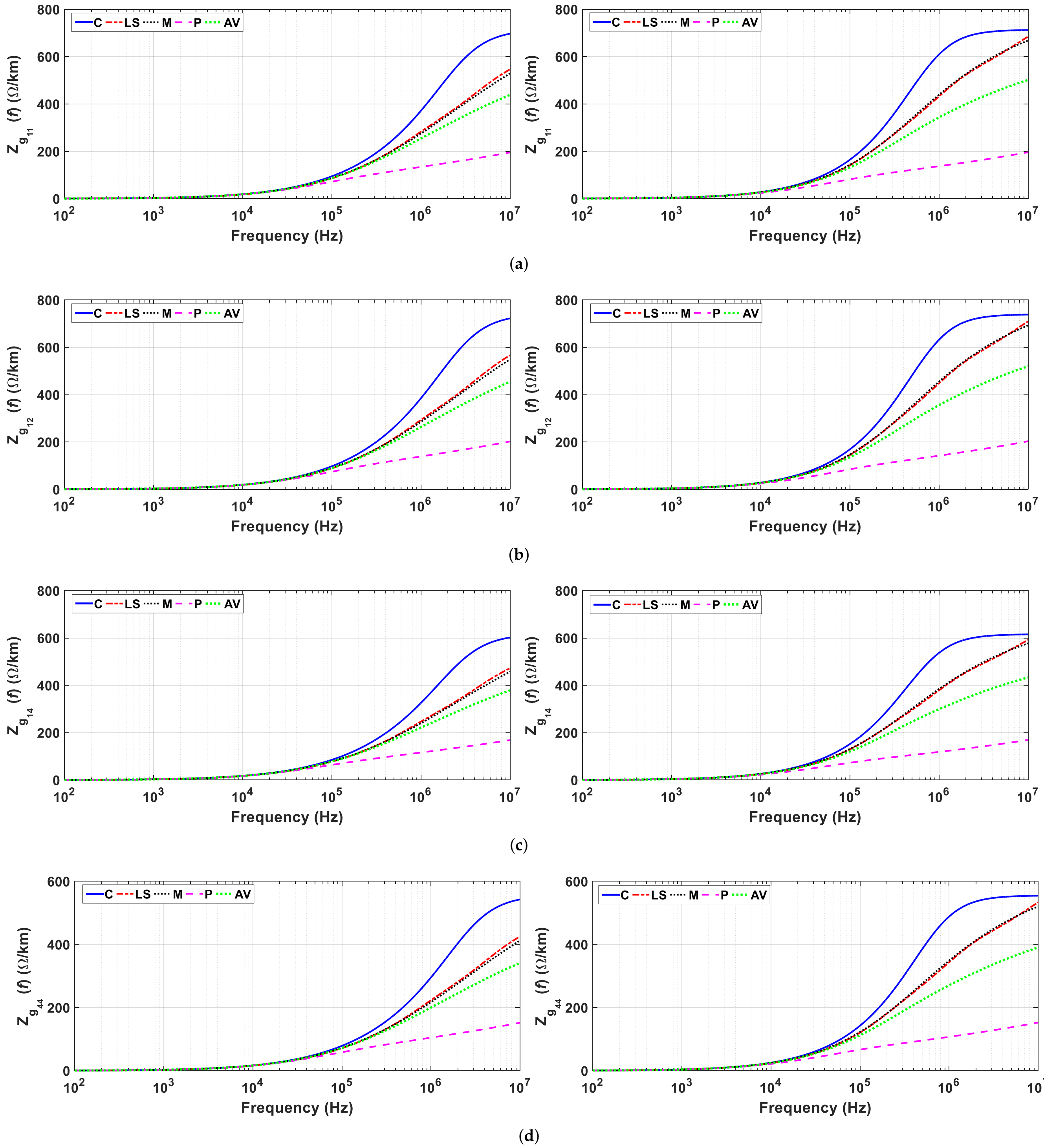

Figure 7. Magnitude of the ground-return impedance for a soil of 700 Ω·m (**left**) and 4000 Ω·m (**right**): (**a**) $Z_{g_{11}}$; (**b**) $Z_{g_{12}}$; (**c**) $Z_{g_{14}}$ and (**d**) $Z_{g_{44}}$.

As seen in this figure, in the range of 100 Hz to 100 kHz, the elements present the same response for all the FD soil approaches studied. Above 100 kHz, the ground-return impedance increases significantly, especially for the high-resistive soil of 4000 Ω·m and the LS, M, and AV models. It can be also noted that the frequency-constant soil using the Nakagawa (C) model provides higher ground-return impedance values than those computed for all the FD soil models and, as the soil resistivity increases, the curve tends to its maximum for frequencies below 2 MHz. On the other hand, when the FD soil model is included, the magnitudes of ground-return impedance are lower compared with those calculated by Nagakawa (C). In this context, the Portela (P) model has presented the lowest values in this frequency range which the differences between the (P) and (C) increases with the increasing frequency. This strong deviation is due to the lack of reliability in the formulas from the Portela (P) model as stated in [23]. This behaviour will influence the transient voltage responses as further detailed. The ground-return admittance elements are shown in Figure 8 for soils of 700 Ω·m (on the left) and 4000 Ω·m (on the right).

As depicted in this figure, the results presented for a frequency range from 100 Hz to 500 kHz, and the differences between the formulations are negligible. However, above 500 kHz, the ground-return admittances computed with Portela (P) have presented a pronounced increase compared with other FD soil models (LS, M and AV). Furthermore, the ground-return admittance with Nakagawa frequency-constant (C) soil has presented a much lower variation in comparison with all FD soil models, showing the importance of considering this type of ground for the proper modeling of OHTL.

The impact of the FD soil models were also analysed in the modal domain. For this, the 5×5 longitudinal impedance and transversal admittance matrices are calculated utilizing (1) and (2). Applying the Kron's reduction from (50) and (51), it yields the 3×3 reduced matrices given by

$$\boldsymbol{Z}'_{\ell}(\omega) = \begin{bmatrix} Z_{11} & Z_{12} & Z_{13} \\ Z_{21} & Z_{22} & Z_{23} \\ Z_{31} & Z_{32} & Z_{33} \end{bmatrix}, \quad \boldsymbol{Y}_{\mathrm{t}}{}'(\omega) = \begin{bmatrix} Y_{11} & Y_{12} & Y_{13} \\ Y_{21} & Y_{22} & Y_{23} \\ Y_{31} & Y_{32} & Y_{33} \end{bmatrix}. \tag{52}$$

Finally, to convert from the phase to the modal domain, a 3×3 modal transformation matrix variable with the frequency are obtained using the Newton-Raphson method as proposed in [46]. Then, using (38) and (39), the $\boldsymbol{Z}'_{\ell}(\omega)$ and $\boldsymbol{Y}_{\mathrm{t}}{}'(\omega)$ are decoupled into three exact modes, named here as α, β and 0, as follows

$$\boldsymbol{Z}_{\mathrm{m}}(\omega) = \begin{bmatrix} Z_{\alpha} & 0 & 0 \\ 0 & Z_{\beta} & 0 \\ 0 & 0 & Z_0 \end{bmatrix}, \quad \boldsymbol{Y}_{\mathrm{m}}(\omega) = \begin{bmatrix} Y_{\alpha} & 0 & 0 \\ 0 & Y_{\beta} & 0 \\ 0 & 0 & Y_0 \end{bmatrix}. \tag{53}$$

The modal impedances for the four FD soil models (LS, M, P and AV) and constant soil (C) considering two soil resistivities of 700 Ω·m and 4000 Ω·m are depicted in Figure 9. As seen in this figure, for the analyzed frequency range, the differences between the FD soil formulations are negligible. However, the impedance of mode 0 Z_0 presents an expressive increase as of 500 kHz, followed by Z_{β} and Z_{α}. The modal admittances are illustrated in Figure 10. As shown in this figure, the distinct FD soil approaches have no major impact on a certain mode. The modal admittance will increase expressively with the increasing frequency where the mode $\alpha - Y_{\alpha}$ has presented the highest value followed by Y_{β} and Y_0.

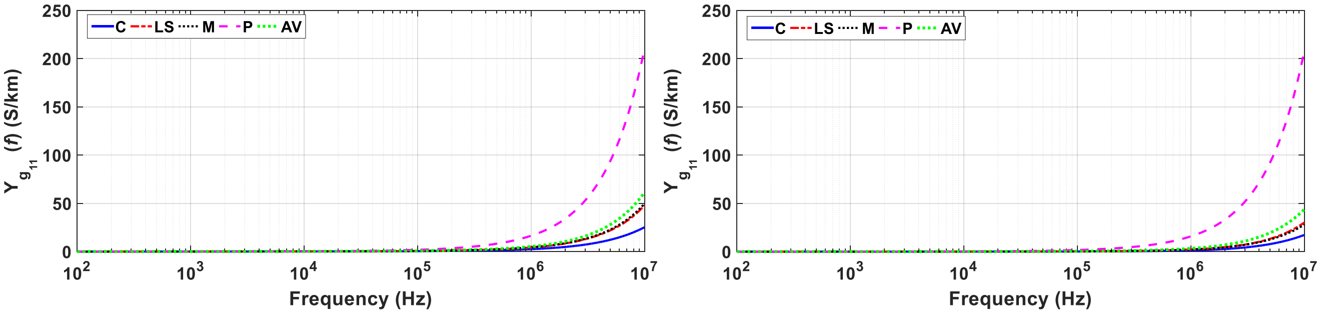

(**a**)

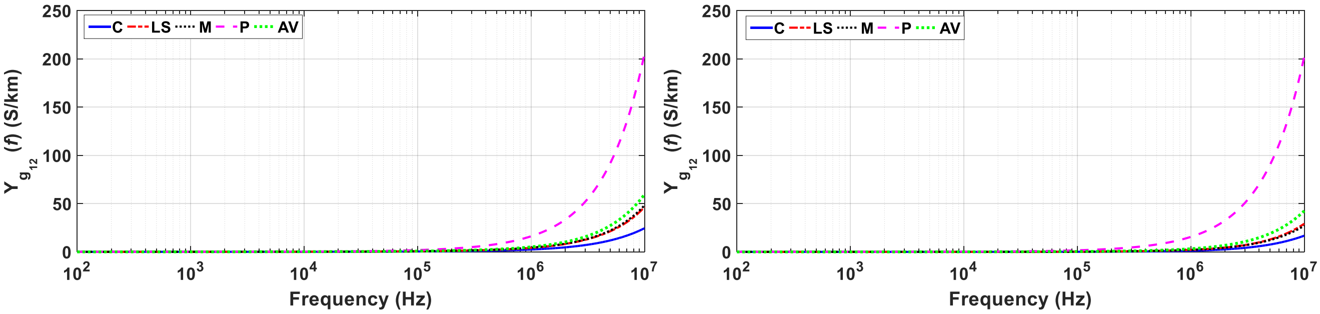

(**b**)

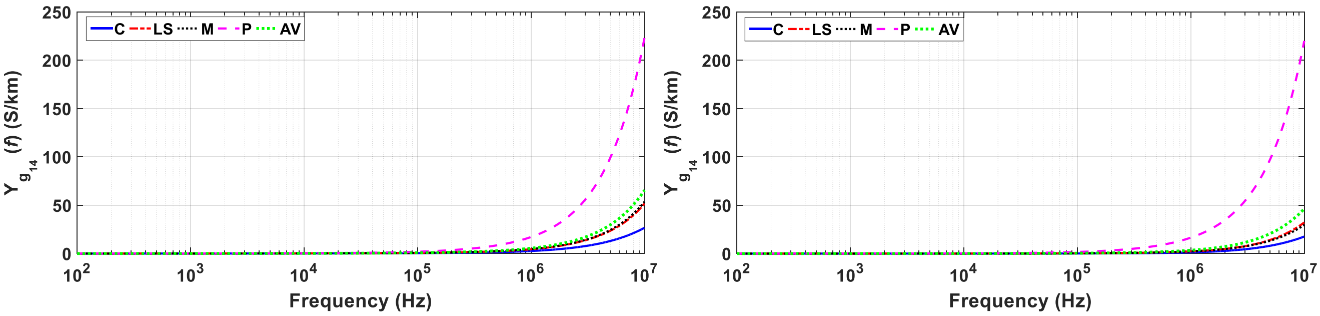

(**c**)

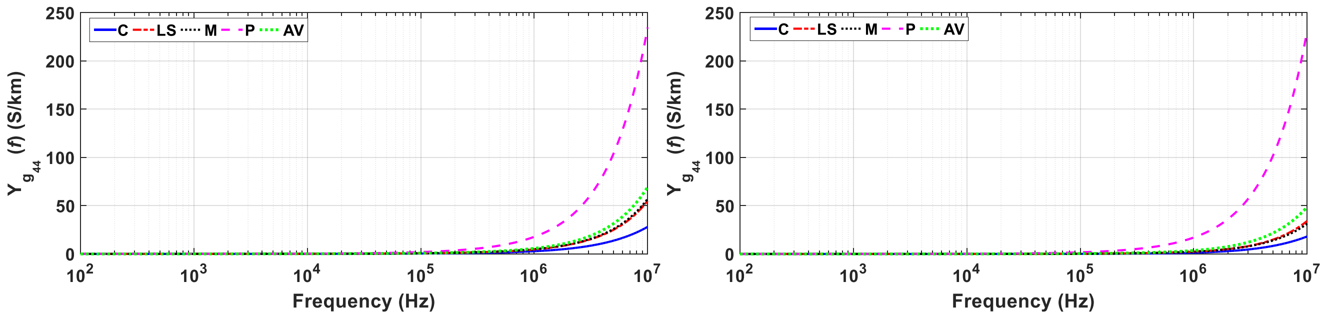

(**d**)

Figure 8. Magnitude of the ground-return admittance for a soil of 700 Ω·m (**left**) and 4000 Ω·m (**right**): (**a**) $Y_{g_{11}}$; (**b**) $Y_{g_{12}}$; (**c**) $Y_{g_{14}}$ and (**d**) $Y_{g_{44}}$.

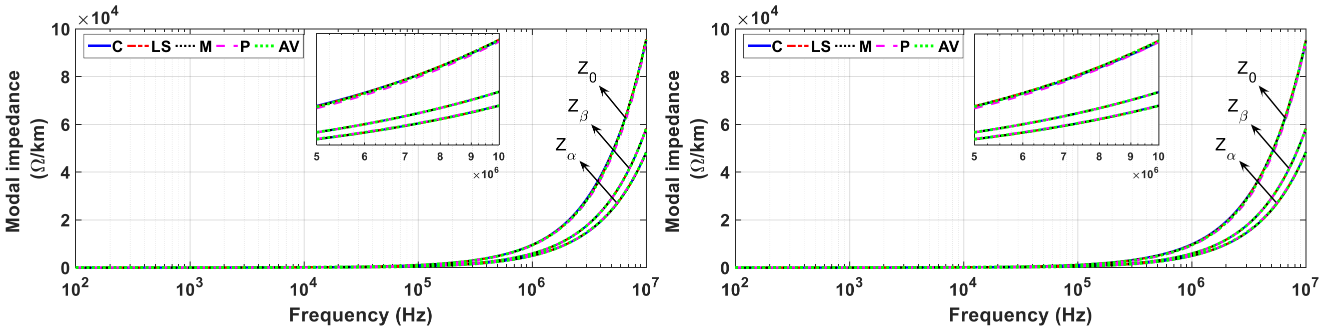

(a) (b)

Figure 9. Magnitude of the modal impedance for a soil of: (**a**) 700 Ω·m and (**b**) 4000 Ω·m.

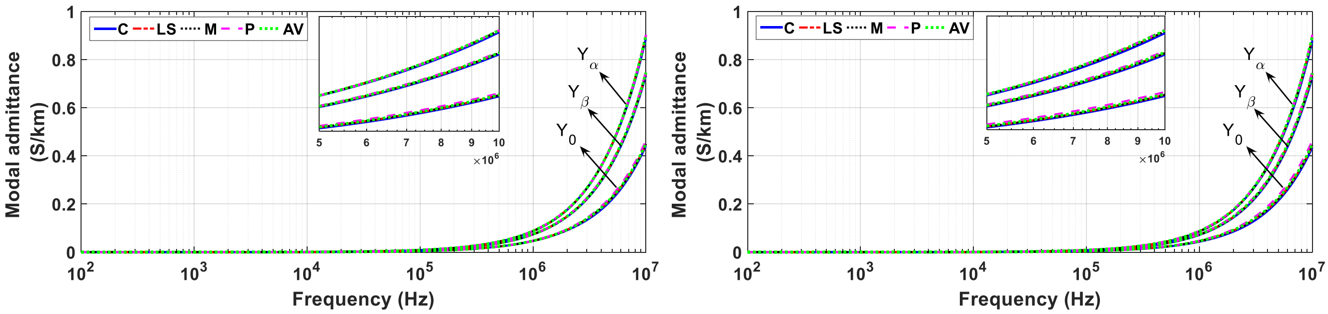

(a) (b)

Figure 10. Magnitude of the modal admittance for a soil of: (**a**) 700 Ω·m and (**b**) 4000 Ω·m.

In this section, two studies are carried out: First, the FD ground-return impedance and ground-return admittance in the frequency-domain. The second is related to the modal impedance Z_{m} and modal admittance Y_{m}, both in the frequency-domain. The modal decomposition allows the interpretation of attenuation constant and propagation velocity in each mode which affect the phase-domain responses. As advantages, the modal decomposition takes into account the FD elements in the impedance and admittance matrices of a given OHTL. This method includes the p.u.l resistance considering the skin effect and the ground-return impedance and admittance assuming FD soil resistivity and permittivity. The influence of the FD can be better visualized using the modal decomposition associated with the NILT methods.

7.2. Attenuation Constant and Propagation Velocity

In this subsection, we carried out the simulations concerning the FD soil models on the attenuation constant $\lambda_{\mathrm{m}}(\omega)$ (43) and the propagation velocity $\mathrm{v}_{\mathrm{m}}(\omega)$ (44) in the modal domain. To this analysis, the $\lambda_{\mathrm{m}}(\omega)$ and $\mathrm{v}_{\mathrm{m}}(\omega)$ are computed for the low-frequency resistivity of 700 and 4000 Ω·m considering the several approaches. The modal constant attenuation for α, β and 0 are illustrated in Figure 11.

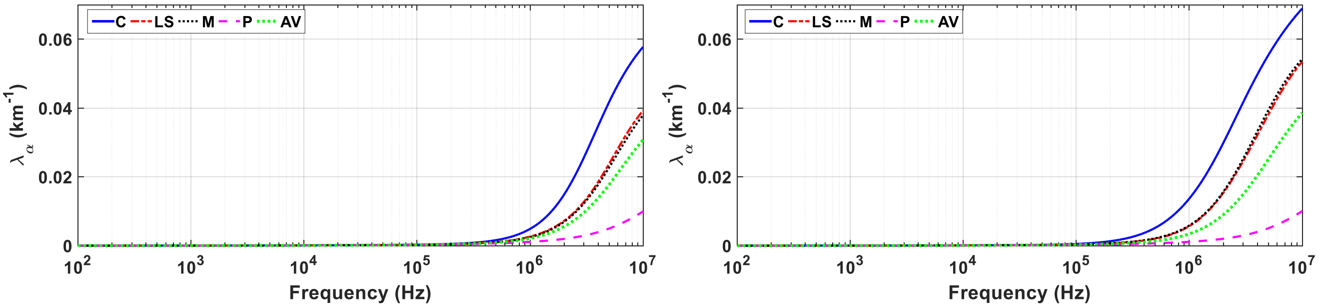

(**a**)

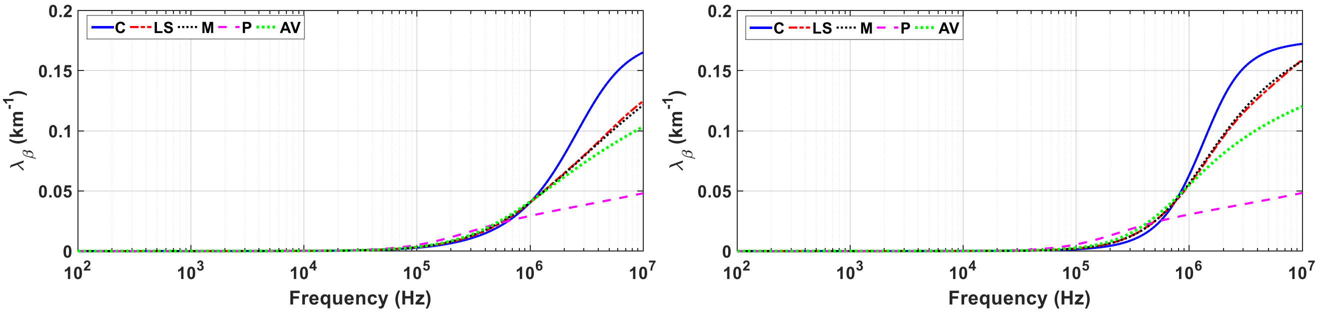

(**b**)

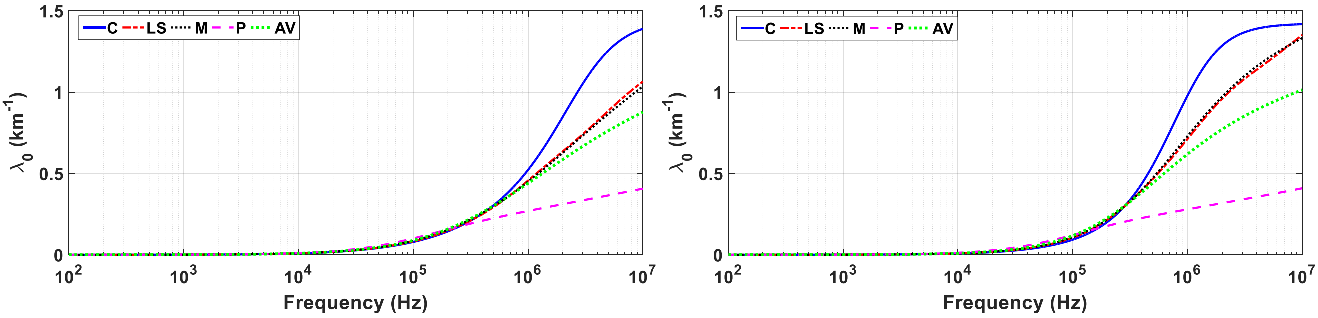

(**c**)

Figure 11. Attenuation constant for a soil of 700 Ω·m (**left**) and 4000 Ω·m (**right**): (**a**) mode α; (**b**) mode β and (**c**) mode 0.

As noted in Figure 11a, the attenuation constant λ_α increases with the increasing frequency for all soil models where the difference between the considered soil models are relevant above a certain frequency (1 MHz). It can be seen that the frequency-constant soil model (C) provided higher value of the attenuation constant whereas the Portela (P) will present the lower values for all frequency range. The attenuation constant λ_β (Figure 11b) has presented similar behavior up to 1 MHz approximately for the soils of 700 and 4000 Ω·m, respectively. Above this frequency, the values obtained for the Portela (P) model are lower than those obtained for the other models. Furthermore, as the soil resistivity increases, the differences between the curves obtained with constant and FD-soil model become more pronounced for frequencies above 1 MHz. Finally, the values of λ_0 (Figure 11c) are similar up to 300 kHz for the FD soil of 700 Ω·m and up to 200 kHz for the FD soil of 4000 Ω·m, where the frequency-constant (C) soil are higher than the other FD soil models. The differences between the models using constant or FD soils become more noticeable above the mentioned frequency, especially for high-resistive soils. The constant attenuation obtained by the Portela (P) model for all propagation modes are much lower than the other soil models. Moreover, the differences between the Portela (P) and the other models increases as the soil resistivity ρ_0 increases. As a consequence, this expressive difference from the Portela (P) model occurs due its strong variation in the soil parameters in (16) and (17) obtained from measurements to determine the variables α' and Δ_i which lacks reliability [23]. Based on these results, the Portela (P) model tends to produce less attenuated voltage waves in the time-domain responses. The modal velocities for the modes α, β and 0 as a function of the frequency are depicted in Figure 12.

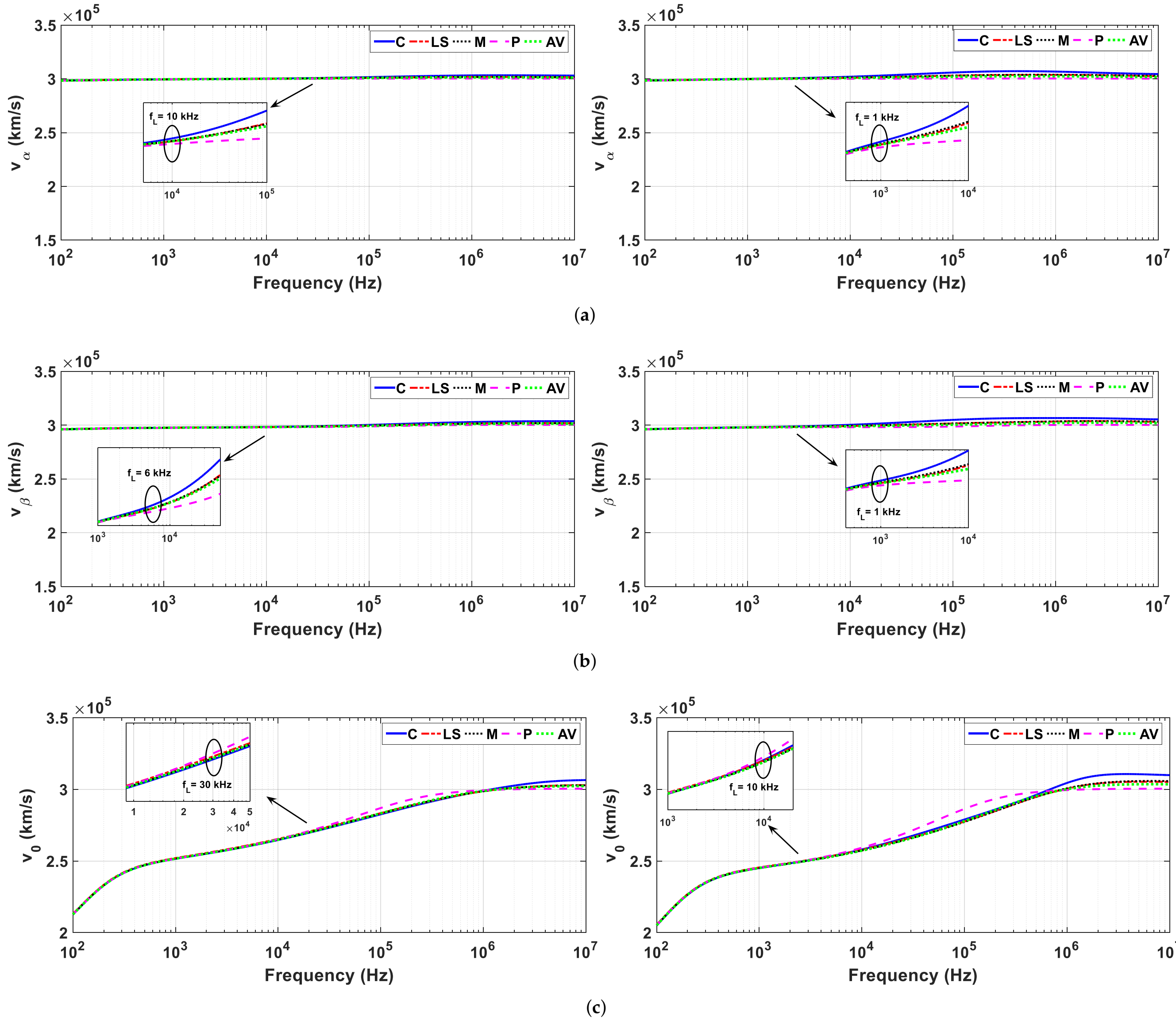

Figure 12. Phase velocity for a soil of 700 Ω·m (**left**) and 4000 Ω·m (**right**): (**a**) mode α; (**b**) mode β and (**c**) mode 0.

According to the results in this figure, the propagation velocities v_α and v_β have no significant difference for both soil models in this frequency range. For the mode 0, the propagation velocity v_0 presents an expressive variation from 100 Hz up to 10 MHz. As indicated, all curves converge to the similar values when a low-resistivity soil is used. However, a slight variation is observed when the Portela (P) model is used above 10 KHz and this difference between the curves increases as the soil resistivity increases. As a consequence, this mode propagates faster depending on the frequency range of the disturbance which will be determinant on the transient waveform.

These divergent characteristics on the modal attenuation constant and modal propagation velocity result into a significant impact on the transient responses on an OHTL subjected to lightning strikes as described in the next section.

7.3. Transient Voltages for the Lightning Direct Strike

In order to investigate the influence of the FD soil models on transient responses developed by a lightning strike, the voltages on phase conductors of two the OHTLs with lengths of 1 km and 10 km are analyzed. The configuration of the studied OHTL is illustrated in Figure 6. This lightning strike is representative of a subsequent return stroke modelled by an impulsive current source expressed by Heidler's function given by [54]

$$i(t) = \frac{I_0}{\eta} \frac{(t/\tau_1)^n}{1+(t/\tau_1)^n} e^{-t/\tau_2}, \tag{54}$$

$$\eta = \exp\left[-\left(\frac{\tau_1}{\tau_2}\right)\left(n\frac{\tau_2}{\tau_1}\right)\right]^{1/n}, \tag{55}$$

where I_0 [A] is the peak current, τ_1 and τ_2 [s] are the front and decay time constants, respectively. The n and η are the steepness and peak correction factors, respectively [55].

The Heidler's function requires a complex integration in the frequency domain for the Fourier transform. In [56], the authors present an analytical formula to compute the frequency spectrum of the Heidler's function. On the other hand, a helpful approach based on close-form expressions to assess the frequency spectrum are given by some authors such as [57–60]. One of these closed-form expressions is presented by Terespolsky and Nixon which is given by [55]

$$i(t) = \frac{I_0}{\eta}\left(1 - e^{-\omega_0 t}\left(\sum_{i=0}^{n_a} \frac{\omega_0^i t^i}{i!}\right)\right) e^{\frac{-t}{\tau_2}}, \tag{56}$$

where ω_0 [rad/s] is the angular frequency associated with the front time and n_a is a steepness factor in this approximation. Applying the Fourier Transform in (56), the frequency-domain current $I(s)$ for this lightning discharge is given by [54]

$$I(s) = \frac{I_0}{\eta} \frac{1}{s+\frac{1}{\tau_2}} \frac{1}{\left(\frac{s+\frac{1}{\tau_2}}{\omega_0}+1\right)^{n_a}}. \tag{57}$$

This work employs the *subsequent stroke* proposed by the [55] with a front time of 0.25 μs and a decay time of 100 μs. The values used in (54)–(56) to generate this lightning subsequent stroke of Heidler and its approximated form are given in the Table 4.

Table 4. Parameters in (54) and (56) to generate the lightning subsequent stroke modeled by the Heidler's function and its approximation [55].

Parameters	Heidler	Approximation
I_0 [kA]	10	10
η	0.993	0.993
n_a	-	33
n	10	-
ω_0 [rad/s]	-	74,000,000
τ_1 [μs]	0.454	-
τ_2 [μs]	143	143

The normalized lightning current waveform and its normalized frequency spectrum are detailed in Figure 13. The transient voltages are computed considering that the lightning strikes at the sending end of phase 1, whereas the other sending ends (phases 2 and 3) are short-circuited. The receiving ends are left open-circuit, as depicted in Figure 14.

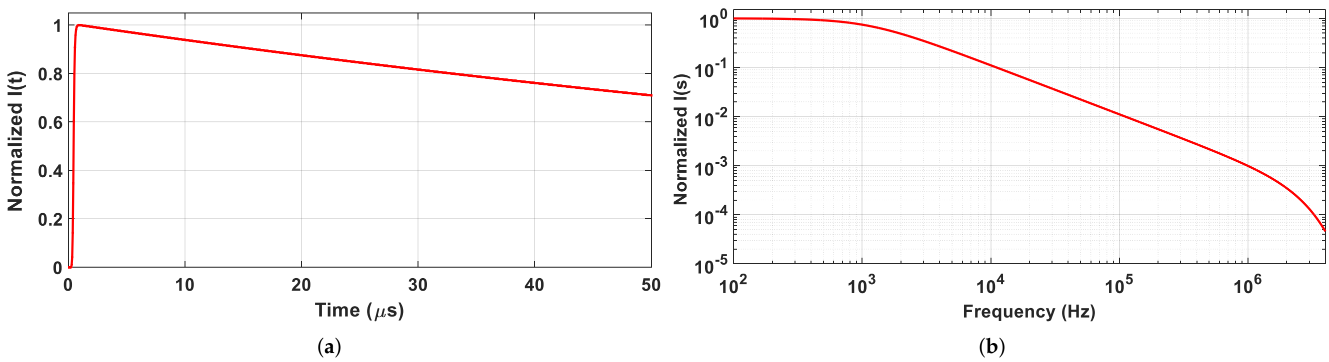

Figure 13. Lightning current injected at the OHTL: (**a**) Time-domain and (**b**) Frequency-domain spectrum.

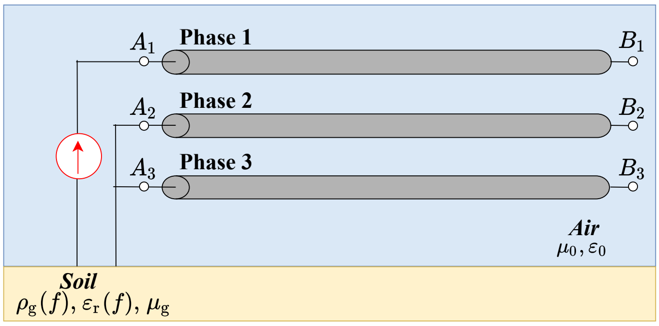

Figure 14. Lightning striking at phase 1 for an open-circuit receiving end.

In order to quantity the influence of the FD soil models at the receiving end voltages, the modal voltages at this terminal are investigated as a function of the frequency for the modes α, β and 0 using (46) for both line lengths (1 and 10 km). The frequency-domain voltages at the receiving end B for the mode α (V_α) are depicted in Figure 15, for the mode β (V_β) are depicted in Figure 16 and for the mode 0 (V_0) are illustrated in Figure 17.

According to the results from Figures 15 and 17, the voltages V_α and V_0 decrease with the increasing frequency and the differences between the FD model curves are negligible. On the other hand, due to the symmetry in the vertical plan of the OHTL, the voltages V_β are zero to all frequency domain. However, to quantify the impact of the FD soil models on the modal voltages, the normalized root-mean-square deviation (NRMQD) $\chi(\%)$ is calculated as follows

$$\chi(\%) = \frac{1}{\Delta_V}\sqrt{\frac{\sum_{i=1}^{N_F}(V_C - V_{FD})^2}{N_F}} \times 100\%, \tag{58}$$

where V_C and V_{FD} are the frequency-domain voltages obtained with frequency-constant and voltages computed with each FD soil model, respectively. The N_F is the number of points in the frequency range (N_F = 10,000, $\Delta_V = V_{max} - V_{min}$ is the difference between the maximum (V_{max}) and minimum (V_{min}) values of the voltage response obtained with the frequency-constant model which is considered as the reference due its more conservative approach on the results. In this analysis, C is considered as the reference due to the conservative approach based on the frequency-constant soil parameters. The values of $\chi(\%)$ for modes α, β and zero are organized in Tables 5–7, respectively.

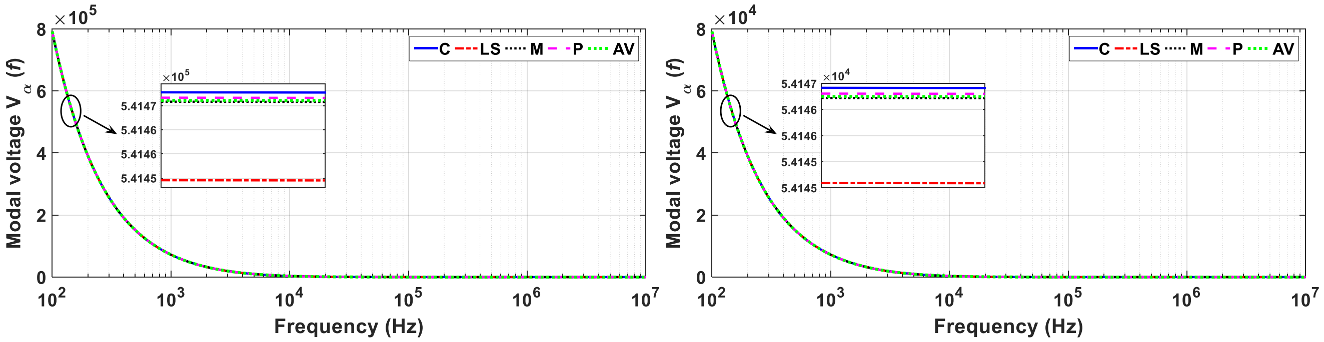

(**a**)

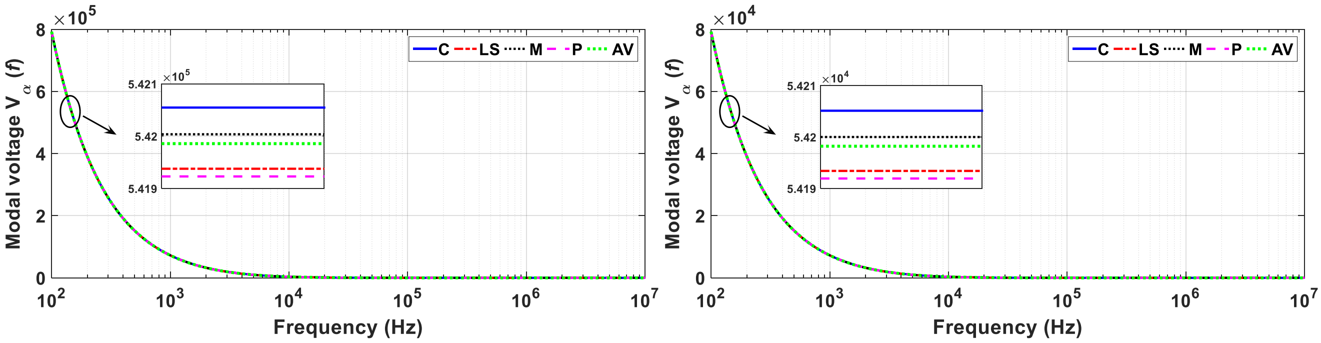

(**b**)

Figure 15. Transient voltages at the receiving end of mode α obtained for the lightning direct strike for the 1 km OHTL (**left**) and 10 km OHTL (**right**) with ρ_0 of: (**a**) 700 Ω·m and (**b**) 4000 Ω·m.

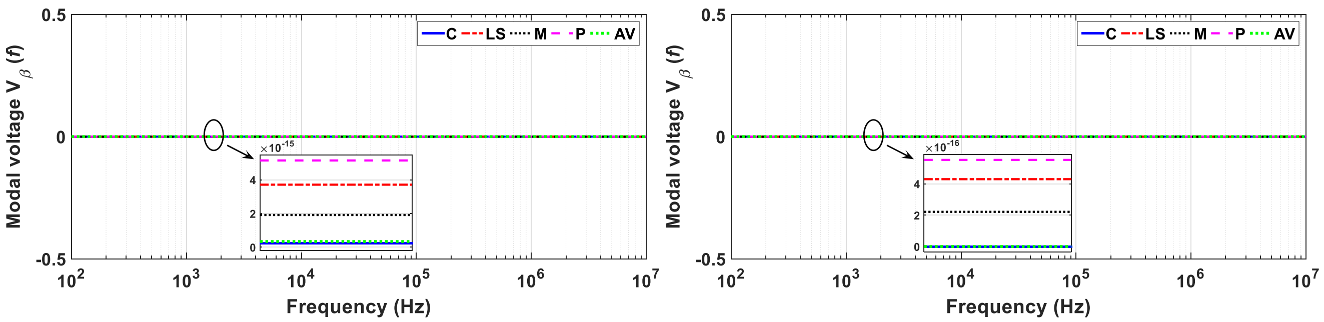

(**a**)

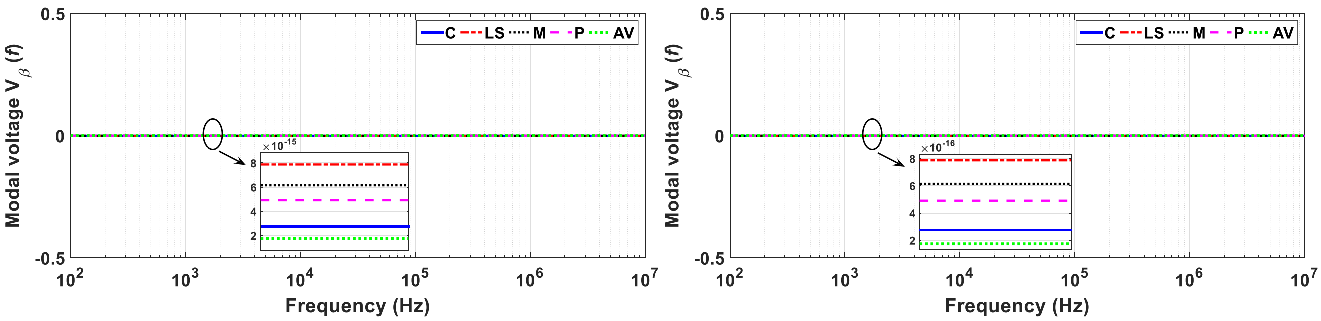

(**b**)

Figure 16. Transient voltages at the receiving end of mode β obtained for the lightning direct strike for the 1 km OHTL (**left**) and 10 km OHTL (**right**) with ρ_0 of: (**a**) 700 Ω·m and (**b**) 4000 Ω.m.

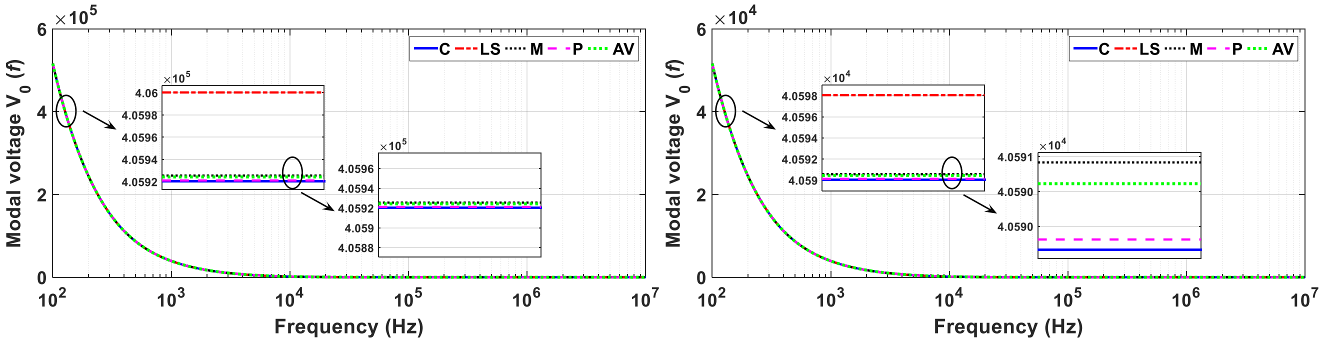

(**a**)

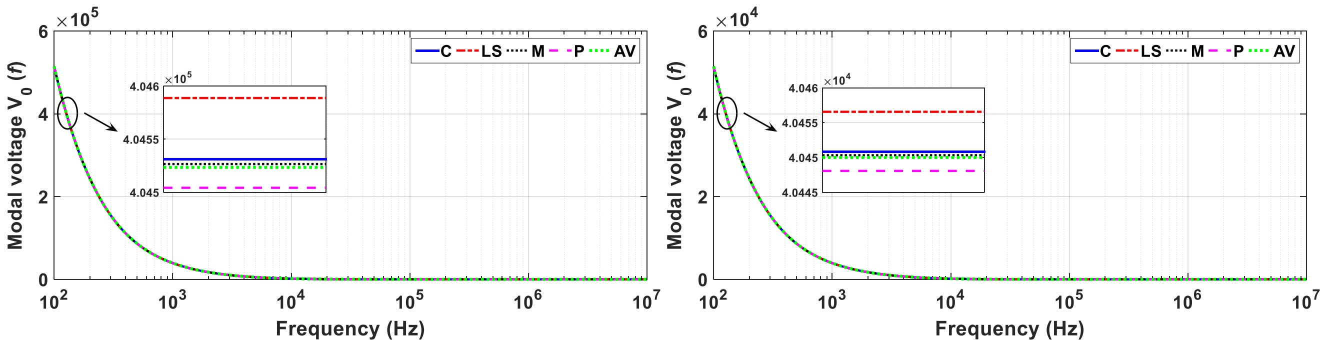

(**b**)

Figure 17. Transient voltages at the receiving end of mode 0 obtained for the lightning direct strike for the 1 km OHTL (**left**) and 10 km OHTL (**right**) with ρ_0 of: (**a**) 700 Ω·m and (**b**) 4000 Ω·m.

Table 5. $\chi(\%)$ for the frequency-domain voltage V_α in mode α for the considered FD soil models.

	ρ = 700 Ω·m		ρ = 4 kΩ·m	
Model	ℓ = 1 km	ℓ = 10 km	ℓ = 1 km	ℓ = 10 km
LS	0.97783×10^{-3}	0.97769×10^{-3}	6.5355×10^{-3}	6.5351×10^{-3}
M	0.25879×10^{-3}	0.25896×10^{-3}	3.7919×10^{-3}	3.7916×10^{-3}
P	0.35506×10^{-3}	0.35674×10^{-3}	9.4411×10^{-3}	9.4416×10^{-3}
AV	0.25744×10^{-3}	0.25773×10^{-3}	5.1607×10^{-3}	5.1605×10^{-3}

Table 6. $\chi(\%)$ for the frequency-domain voltage V_β in mode β for the considered FD soil models.

	ρ = 700 Ω·m		ρ = 4 kΩ·m	
Model	ℓ = 1 km	ℓ = 10 km	ℓ = 1 km	ℓ = 10 km
LS	11.132×10^{-5}	11.519×10^{-5}	8.9062×10^{-5}	8.224×10^{-5}
M	10.892×10^{-5}	11.268×10^{-5}	8.78862×10^{-5}	8.1312×10^{-5}
P	10.871×10^{-5}	11.204×10^{-5}	8.5796×10^{-5}	7.9529×10^{-5}
AV	10.906×10^{-5}	11.260×10^{-5}	8.831×10^{-5}	8.1988×10^{-5}

As described in Tables 5–7, the NRMQD $\chi(\%)$ obtained for the modes α, β and 0 are significantly small for all frequency range. However, the NRMQD $\chi(\%)$ for the mode β can be neglected for the practical analysis. Concerning the results in Tables 5 and 7, one notes that NRMQD $\chi(\%)$ for the Portela (P) model for both line lengths and the high-resistivity soil, is much higher in comparison to the other FD models. Nevertheless, the Longmire-Smith (LS) model has presented high values of NRMQD $\chi(\%)$ for the soil of 700 Ω·m, as expected from the Figures 15a and 17a (see the zoom of these figures). According to these figures, the Longmire-Smith (LS) model is higher at the low frequencies. This is a consequence of the low-frequency resistivity ρ_0 is the lowest from the other FD soil models as shown in Tables 2 and 3 as presented in the Section 3.

Table 7. $\chi(\%)$ for the frequency-domain voltage V_0 in mode 0 for the considered FD soil models.

	ρ = 700 Ω·m		ρ = 4 kΩ·m	
Model	ℓ = **1 km**	ℓ = **10 km**	ℓ = **1 km**	ℓ = **10 km**
LS	4.7781×10^{-3}	4.8279×10^{-3}	2.9125×10^{-3}	2.9309×10^{-3}
M	0.33281×10^{-3}	0.30928×10^{-3}	0.96688×10^{-3}	1.1147×10^{-3}
P	0.22058×10^{-3}	0.52569×10^{-3}	3.2271×10^{-3}	3.6211×10^{-3}
AV	0.24804×10^{-3}	0.23119×10^{-3}	1.3907×10^{-3}	1.6173×10^{-3}

The time-domain voltages V_1^B, V_2^B and V_3^B are calculated applying the NILT method on (47), where the phase-domain responses are computed using the *Lanczos's window function* and 2500 samples in the frequency domain. The time-domain voltages produced by the lightning strike for the 1 km and 10 km OHTLs on soils of 700 Ω·m and 4000 Ω·m on the phase 1 are illustrated in Figure 18.

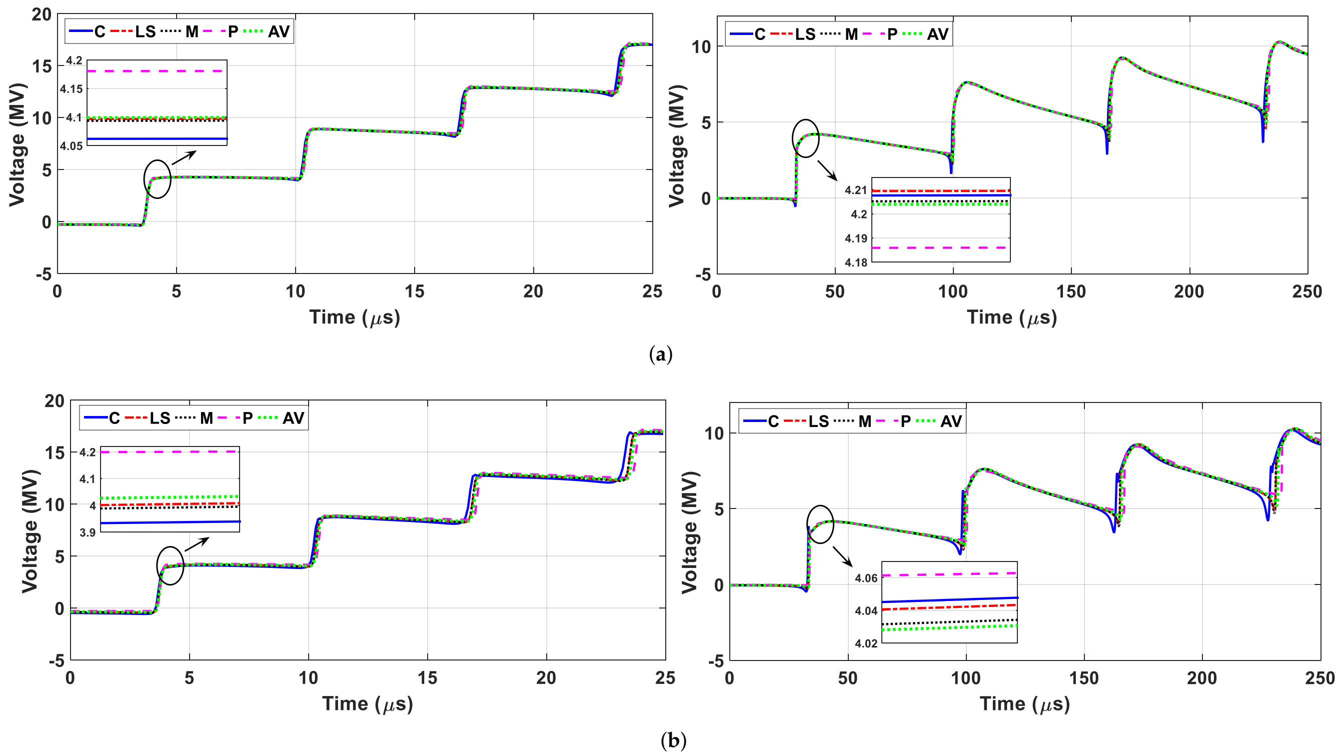

Figure 18. Transient voltages at the receiving end of phase 1 V_1^B obtained for the lightning direct strike for the 1 km OHTL (**left**) and 10 km OHTL (**right**) with ρ_0 of: (**a**) 700 Ω·m and (**b**) 4000 Ω.m.

According to the Figure 18, the transient voltages generated for the lightning strike present multiple peaks due to the reflections between the sending and open receiving ends. Furthermore, the voltage peaks are lower for the longer line length due to the losses associated p.u.l equivalent resistance that increases as the soil resistivity increases. Concerning the voltage waveforms, the responses in phase 1 are similar for all considered FD soil models when a ground resistivity of 700 Ω·m is assumed, as depicted in Figure 18a. However, for voltage waveforms associated with high-resistive soil in Figure 18b, small differences can be noted for the frequency-constant (C) model in relation to those responses form FD soil models. In this case, a small delay is observed for the between the curves where the peaks with the frequency-constant soil occurs slightly before than those obtained with FD soil models. The lightning-induced voltages produced on the phases 2 (or on phase 3) are depicted in Figure 19.

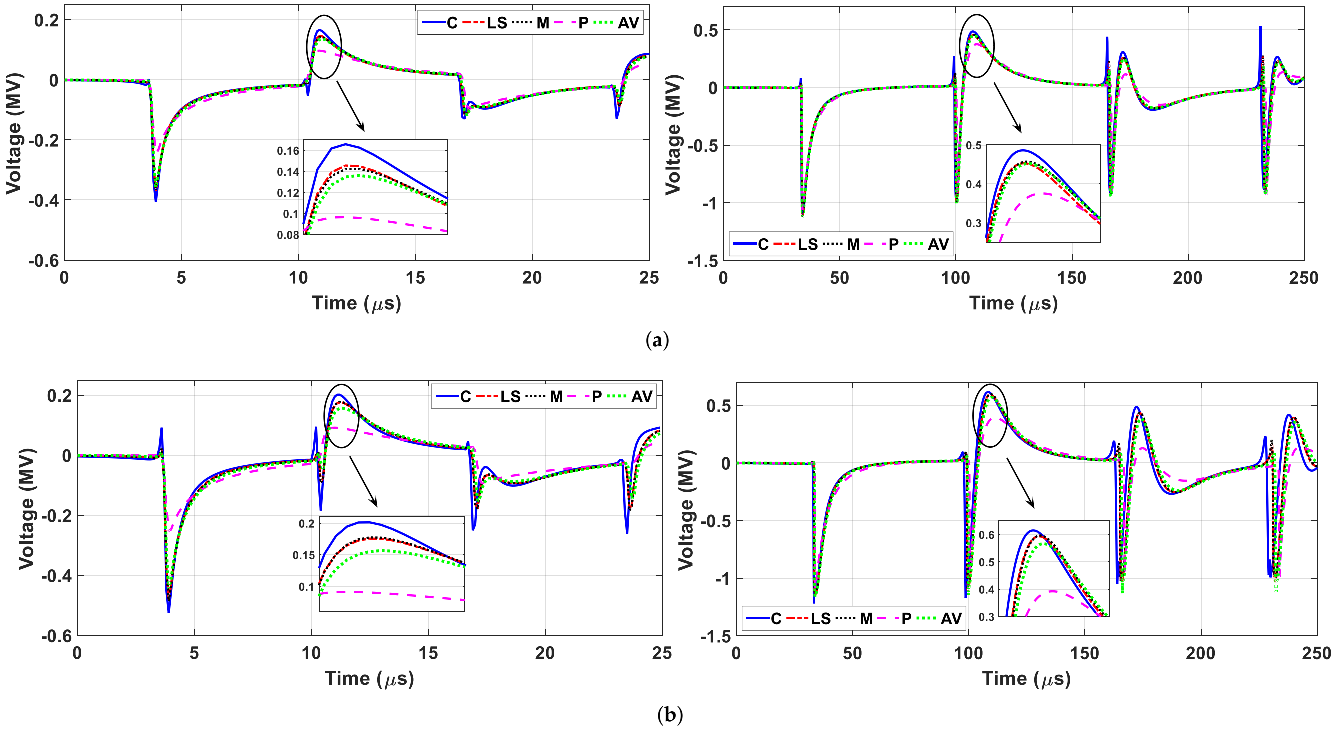

Figure 19. Transient voltages at the receiving end of phase 2 V_2^{B} and phase 3 V_3^{B} obtained for the lightning direct strike for the 1 km OHTL (**left**) and 10 km OHTL (**right**) with ρ_0 of: (**a**) 700 Ω·m and (**b**) 4000 Ω.m.

By analyzing the voltage waveforms, one notes that the frequency effect on the soil electrical parameters has a major impact on the lightning-induced voltages. It can be seen that the frequency-constant (C) soils produce higher voltage peaks in comparison with those obtained for the FD soil models. Furthermore, the differences in the voltage peaks are also followed by a delay between the curves. Simulation results have shown that the Portela (P) model has presented the highest difference in the voltage waveforms, especially at the peaks, whereas the Longmire-Smith (LS), Messier (M) and Alípio-Visacro (AV) tends to produce similar responses. To quantify the differences between the responses from the two types of soil models in the time-domain responses, the percent deviation $\epsilon(\%)$ is calculated as follows

$$\epsilon(\%) = \frac{V_{\mathrm{p}}^{C} - V_{\mathrm{p}}^{\mathrm{FD}}}{V_{\mathrm{p}}^{C}} \times 100\%, \tag{59}$$

where V_{p}^{C} is the voltage peak obtained considering the frequency-constant (C) soil and $V_{\mathrm{p}}^{\mathrm{FD}}$ is the voltage peak computed with each FD soil model. The percentage error is computed based on voltage peaks shown in detail for each simulation are organized in Table 8 for the phase 1 and in Table 9 for the phases 2 and 3.

As seen in Table 8, the percentage deviation is small and it decreases for the increasing line length, however, it increases as the soil resistivity becomes higher. However, regarding the lightning-induced voltages in Table 9, the percentage deviation is very pronounced, especially, for high-resistive soil obtained for Portela (P) model, as highlighted in cyan. As a consequence of considerable difference, the ground-return impedance and admittance parameters must be properly calculated combining an adequate FD soil model [23]. The voltages across the insulator strings generated during a lightning strike can be significantly modified for the distinct FD soil model or even between the frequency-constant (C). Then, the assessment for the occurrence of backflashover could be affected in transient analysis [2]. To extend our analysis, the NRMQD $\delta(\%)$ for the time-domain voltages is calculated as given by

$$\delta(\%) = \frac{1}{\Delta_C}\sqrt{\frac{\sum_{i=1}^{N_T}(V_C - V_{FD})^2}{N_T}} \times 100\%, \tag{60}$$

where V_C and V_{FD} are voltages obtained frequency-constant (C) model and voltages computed with each FD soil models, respectively. The N_T is the number of points in the time range (N_T = 2500), $\Delta_C = V_{max} - V_{min}$ is the difference between the maximum (V_{max}) and minimum (V_{min}) values of the voltage response with C. The computed NRMQD $\delta(\%)$ is organized in Tables 10 and 11 for phase 1 and phases 2 and 3, respectively.

Table 8. $\epsilon(\%)$ for the FD soil models (phase 1).

	ρ = 700 Ω·m		ρ = 4 kΩ·m	
Model	**ℓ = 1 km**	**ℓ = 10 km**	**ℓ = 1 km**	**ℓ = 10 km**
LS	0.75	0.023	1.81	0.12
M	0.68	0.071	1.46	0.34
P	2.45	0.52	6.31	0.34
AV	0.77	0.095	2.34	0.41

Table 9. $\epsilon(\%)$ for the FD soil models (phases 2 and 3).

	ρ = 700 Ω·m		ρ = 4 kΩ·m	
Model	**ℓ = 1 km**	**ℓ = 10 km**	**ℓ = 1 km**	**ℓ = 10 km**
LS	12.24	6.87	14.17	6.09
M	14.23	6.27	13.27	6.53
P	41.76	27.00	54.75	44.69
AV	18.75	7.61	25.06	13.79

Table 10. $\delta(\%)$ for the FD soil models (phase 1).

	ρ = 700 Ω·m		ρ = 4 kΩ·m	
Model	**ℓ = 1 km**	**ℓ = 10 km**	**ℓ = 1 km**	**ℓ = 10 km**
LS	1.189	2.23	2.6049	4.3194
M	1.2632	2.3025	2.5378	4.3129
P	2.2916	3.199	4.5027	5.9444
AV	1.496	2.483	3.4222	4.9607

Table 11. $\delta(\%)$ for the FD soil models (phases 2 and 3).

	ρ = 700 Ω·m		ρ = 4 kΩ·m	
Model	**ℓ = 1 km**	**ℓ = 10 km**	**ℓ = 1 km**	**ℓ = 10 km**
LS	1.9433	5.0902	4.2439	9.7088
M	2.0624	5.3715	4.2362	9.882
P	4.7381	7.783	7.6231	12.456
AV	2.5307	5.8437	5.4465	11.509

As noted from Table 10, all the curves presented practically the same behavior for a fixed soil resistivity. However, from Table 11, it can be observed that the responses obtained for the Portela (P) model presented the most expressive NRMQD for the two line lengths, with these values highlighted in cyan. These significant variations occur due to the highest propagation velocity and lowest attenuation constant obtained for the mode 0 with the Portela (P) model. The highest value of NRMQD is found for the shorter line length (1 km) and higher soil resistivity (4000 Ω·m).

It is interesting to note that the FD voltages in the modal domain have not presented pronounced differences for the distinct FD soil models. However, only after applying the NILT method, the differences between each FD soil models on the transient responses, directly in the phase domain, are seen and interpreted.

In all simulations in frequency and time domains carried out in this paper, except for the modal voltages, the Portela (P) model has resulted in the higher difference or more pronounced variation in comparison to the other FD soil models. This pronounced difference occurs due to the highest variation in the soil resistivity calculated by Portela's closed-form expression. However, this formulation lacks of reliability in the measurements of obtained the α' and Δ_i as detailed in [23]. On the other hand, the Longmire-Smith (LS) and Messier (M) models presented similar values of NRMQD which is explained by the reason that both models are based on the measurements realized by Scott [42]. Finally, the Alípio-Visacro (AV) model presented pronounced variation in comparison to those obtained with the frequency-constant (C) model, especially for high-resistive soils. The Alípio-Visacro (AV) model is recommended by CIGRÈ WG C4.33 (see the Table 5.1 in [23]) where, for practical engineering cases involving the OHTLs, the frequency dependence of the soil electrical parameters should be considered for accurate electromagnetic transient analysis.

The modal voltages computed by the LS model presented higher values at the low-frequency range, although its impact on the time-domain responses is very small. This occurs with higher variation in the soil resistivity being more pronounced for the Portela (P) model associated with the high-frequency content of the disturbance injected on the OHTL. As a result, the Portela (P) model has produced the major impact on the time-domain transient responses.

As detailed in this work, the FD soil electrical parameters can lead to significant variations in the voltage waveforms, especially at their voltage peaks. Furthermore, some voltage peaks do not occur at the same time as indicated in the simulations due to distinct propagation velocity in modal domain which impact the time-domain responses and may also affect operation of protection devices and the prediction of backflashovers in power systems. Besides that, the modal-domain analysis allows that the FD soil electrical parameter be included in the ground-return impedance and admittance matrices, and the influence of distinct FD soil models on the attenuation constant and propagation velocity are comprehended, as well as the modal voltages. Once these variables are converted from modal to phase domain, we can better interpret the time-domain responses.

Most of the OHTL models available in the EMT-type programs employ frequency-constant soil parameters to compute the transient responses on power systems. For instance, the ground-return parameters are calculated with the Carson's approach which neglects the displacement currents in the soil, disregards the ground-return admittance and assumes frequency-constant ground parameters (only conductivity) [2,13,14]. These conditions may produce inaccurate transient responses especially for OHTL located on high-resistive soils under high-content disturbances such as lightning [2]. As illustrated in this paper, proper modeling of ground-return ground parameters (impedance and admittance) with Nakagawa's approach combined with the FD soil model has a pronounced impact on the transient caused by lightning strikes.

As the contribution of this paper, distinct and causal FD soil models were considered for the transient analysis. We considered the ground-return admittance for an OHTL with double ground wires whose effects are taken into account by the Kron's reduction. The phase-domain and modal-domain simulations were carried out in time and in frequency domains that were developed with programming code language that can be implemented in toolboxes in MATLAB, other simulation platforms or extended to EMP-type programs, such as ATP-software.

8. Conclusions

This paper has investigated the impact of four causal FD soil models proposed by Longmire-Smith (LS), Messier (M), Portela (P) and Alípio-Visacro (AV) on the transient responses generated by lightning on three-phase OHTL with two ground wires located on soils of 700 and 4000 Ω·m. The frequency range was from 100 Hz to 10 MHz. Modal decomposition technique was employed to better evaluate the differences between the causal FD soil models on the responses.

The ground-return impedance and admittance matrices were calculated using the Nakagawa's approach considering frequency-constant (C) and FD soil models mentioned above. The ground-return impedance and admittance elements have shown a similar behaviour up to a certain frequency. Above this frequency, up to 10 MHz, these elements have presented significant deviations for the FD soil models, especially for the Portela (P) model, which plays a fundamental role in phase and modal variables. The modal impedances Z_m and admittances Y_m have presented similar values between all the FD soil models. On the other hand, modal attenuation of constant λ_{m} and propagation velocity $\mathrm{v_m}$ is influenced by the FD soil model, especially for the mode 0 at the high frequencies for high-resistive soils. The more expressive variations were found for the Portela (P) model. Concerning the modal-domain voltages, the Longmire-Smith (LS) model has presented higher NMQDR for the low-resistivity, whereas the Portela (P) model presented the highest NMQDR for the high-resistivity soil.

The phase-domain voltages on the phase 1 have demonstrated no expressive deviation when the four FD soil models were considered. However, the most significant deviations were obtained for the induced voltages on the phases 2 and 3 with the FD soil model, where the voltage peaks are very much reduced in comparison to those computed by the frequency-constant soil with Nakagawa's approach. The model proposed by Portela (P) have presented the highest deviations especially for a high-resistive of 4000 Ω·m. For practical engineering cases involving the OHTLs above soils of 700 Ω·m, the FD soil model proposed by Alípio-Visacro (AV) should be considered for accurate electromagnetic transient analysis. The observed differences for both types of soils could affect the estimation of the backflashover in power systems under these soil conditions. Besides that, Nakagawa's approach considers several characteristics of soil that are neglected in most of EMT-type tools.

The modal decomposition technique is a interesting tool to investigate the impact of FD soils on the transient responses in OHTLs since valuable information can be extracted in this domain. Results provided in this paper showed that the impact on the transient voltages generated by lightning strikes where the induced voltages have pronounced variations when the FD soil model were considered, especially for OHTL located high-resistivity soils.

Author Contributions: Conceptualization, T.F.G.P., A.R.J.d.A., J.S.L.C., S.K. and J.P.F.; Methodology, T.F.G.P., A.R.J.d.A.; Software, T.F.G.P.; Validation, T.F.G.P., A.R.J.d.A.; Formal Analysis, T.F.G.P., A.R.J.d.A.; Investigation, T.F.G.P., A.R.J.d.A., J.S.L.C.; Writing—original draft preparation, T.F.G.P., A.R.J.d.A., J.S.L.C., S.K. and J.P.F.; Visualization, T.F.G.P., A.R.J.d.A., J.S.L.C.; Supervision, S.K., J.P.F.; Project Administration, S.K., J.P.F.; Funding, S.K., J.P.F. All authors have read and agreed to the published version of the manuscript.

Funding: This work was funded by the Coordenação de Aperfeiçoamento de Pessoal de Nível Superior (CAPES)—Finance code 001 and by São Paulo Research Foundation (FAPESP) (grants: 2019/01396-1, 2020/10141-4 and 2021/06157-5).

Institutional Review Board Statement: Not applicable.

Informed Consent Statement: Not applicable.

Data Availability Statement: Not applicable.

Conflicts of Interest: The authors declare no conflict of interest.

References

1. Pascoalato, T.F.G.; de Araújo, A.R.J.; Colqui, J.S.L.; Kurokawa, S.; Filho, J.P. An Analysis of Frequency-Dependent Soil Models: Influence on the Transient Responses. In Proceedings of the 2021 14th IEEE International Conference on Industry Applications (INDUSCON), Sao Paulo, Brazil, 16–18 August 2021; pp. 1–8. [CrossRef]
2. Diniz, F.A.; Alípio, R.S.; Moura, R.A.R.d. Assessment of the Influence of Ground Admittance Correction and Frequency Dependence of Electrical Parameters of Ground of Simulation of Electromagnetic Transients in Overhead Lines. *J. Control Autom. Electr. Syst.* **2022**, 1–15. [CrossRef]
3. Nguyen, T.; Chan, H. Evaluation of modal transformation matrices for overhead transmission lines and underground cables by optimization method. *IEEE Trans. Power Deliv.* **2002**, *17*, 200–209. [CrossRef]
4. Morched, A.; Gustavsen, B.; Tartibi, M. A universal model for accurate calculation of electromagnetic transients on overhead lines and underground cables. *IEEE Trans. Power Deliv.* **1999**, *14*, 1032–1038. [CrossRef]
5. Nguyen, H.; Dommel, H.; Marti, J. Direct phase-domain modelling of frequency-dependent overhead transmission lines. *IEEE Trans. Power Deliv.* **1997**, *12*, 1335–1342. [CrossRef]
6. Colqui, J.S.; de Araújo, A.R.; Caballero, P.T.; Kurokawa, S. Alternative method using recursive convolution for electromagnetic transient analysis in balanced overhead transmission lines. *IET Sci. Meas. Technol.* **2020**, *14*, 800–807. [CrossRef]
7. Tavighi, A.; Martí, J.; Gutiérrez-Robles, J. Comparison of the FdLine and ULM Frequency dependent EMTP Line Models with a reference Laplace solution. In Proceedings of the Int. Conf. on Power Systems Transients (IPST 2015), Cavtat, Croatia, 15–18 June 2015; pp. 1–8.
8. Papadopoulos, T.A.; Chrysochos, A.I.; Traianos, C.K.; Papagiannis, G. Closed-Form Expressions for the Analysis of Wave Propagation in Overhead Distribution Lines. *Energies* **2020**, *13*, 4519. [CrossRef]
9. Torrez Caballero, P.; Marques Costa, E.C.; Kurokawa, S. Modal decoupling of overhead transmission lines using real and constant matrices: Influence of the line length. *Int. J. Electr. Power Energy Syst.* **2017**, *92*, 202–211. [CrossRef]
10. de Lima, A.C.S.; Portela, C. Inclusion of frequency-dependent soil parameters in transmission-line modeling. *IEEE Trans. Power Deliv.* **2006**, *22*, 492–499. [CrossRef]
11. Tomasevich, M.M.Y.; Lima, A.C. Impact of frequency-dependent soil parameters in the numerical stability of image approximation-based line models. *IEEE Trans. Electromagn. Compat.* **2015**, *58*, 323–326. [CrossRef]
12. De Conti, A.; Emídio, M.P.S. Simulation of transients with a modal-domain based transmission line model considering ground as a dispersive medium. In Proceedings of the IPST'2015—International Conference on Power Systems Transients, Cavtat, Croatia, 15–18 June 2015.
13. Papadopoulos, T.A.; Datsios, Z.G.; Chrysochos, A.I.; Mikropoulos, P.N.; Papagiannis, G.K. Wave Propagation Characteristics and Electromagnetic Transient Analysis of Underground Cable Systems Considering Frequency-Dependent Soil Properties. *IEEE Trans. Electromagn. Compat.* **2020**, *63*, 259–267. [CrossRef]
14. Carson, J.R. Wave propagation in overhead wires with ground return. *Bell Syst. Tech. J.* **1926**, *5*, 539–554. [CrossRef]
15. Nakagawa, M. Admittance correction effects of a single overhead line. *IEEE Trans. Power Appar. Syst.* **1981**, *PAS-100*, 1154–1161. [CrossRef]
16. Liu, Z.; De Silva, H. An efficient analytical based technique to numerical calculation of extended earth return impedance and admittance of overhead lines. *Electr. Power Syst. Res.* **2021**, *197*, 107330. [CrossRef]
17. Kim, I. A New Single-Logarithmic Approximation of Carson's Ground-Return Impedances—Part 1. *IEEE Access* **2021**, *9*, 103850–103861. [CrossRef]
18. Feng, T.; Han, L.; Ma, W.; Dong, X.; Xiao, Z.; Yan, P. A Novel Method for Calculating Ground Return Impedance of Overhead Lines. In Proceedings of the 2019 IEEE 3rd Conference on Energy Internet and Energy System Integration (EI2), Changsha, China, 8–10 November 2019; pp. 1003–1007. [CrossRef]
19. Ametani, A.; Miyamoto, Y.; Baba, Y.; Nagaoka, N. Wave Propagation on an Overhead Multiconductor in a High-Frequency Region. *IEEE Trans. Electromagn. Compat.* **2014**, *56*, 1638–1648. [CrossRef]
20. Theodoulidis, T. On the closed-form expression of Carson's integral. *Period. Polytech. Electr. Eng. Comput. Sci.* **2015**, *59*, 26–29. [CrossRef]
21. Alipio, R.; Visacro, S. Modeling the frequency dependence of electrical parameters of soil. *IEEE Trans. Electromagn. Compat.* **2014**, *56*, 1163–1171. [CrossRef]
22. Cavka, D.; Mora, N.; Rachidi, F. A Comparison of frequency-dependent soil models: Application to the analysis of grounding systems. *IEEE Trans. Electromagn. Compat.* **2014**, *56*, 177–187. [CrossRef]
23. CIGRE C4.33, W.G. *Impact of Soil-Parameter Frequency Dependence on the Response of Grounding Electrodes and on the Lightning Performance of Electrical Systems*; Tech. Brochure 781; 2019; pp. 1–66. Available online: https://e-cigre.org/publication/781-impact-of-soil-parameter-frequency-dependence-on-the-response-of-grounding-electrodes-and-on-the-lightning-performance-of-electrical-systems (accessed on 12 January 2022).
24. Schroeder, M.A.O.; de Barros, M.T.C.; Lima, A.C.; Afonso, M.M.; Moura, R.A. Evaluation of the impact of different frequency dependent soil models on lightning overvoltages. *Electr. Power Syst. Res.* **2018**, *159*, 40–49. [CrossRef]
25. Gertrudes, J.B.; Tavares, M.C.; Portela, C. Transient analysis on overhead transmission line considering the frequency dependent soil representation. In Proceedings of the 2011 IEEE Electrical Power and Energy Conference, Winnipeg, MB, Canada, 3–5 October 2011; pp. 362–367. [CrossRef]

26. Portela;, C.M.; Tavares, M.C.; Filho, J.P. Accurate representation of soil behaviour for transient studies. *IEEE Proc.-Gener. Transm. Distrib.* **2003**, *150*, 736–744. [CrossRef]
27. Moura, R.A.; Schroeder, M.A.; Menezes, P.H.; Nascimento, L.C.; Lobato, A.T. Influence of the soil and frequency effects to evaluate atmospheric overvoltages in overhead transmission lines—Part I: The influence of the soil in the transmission lines parameters. In Proceedings of the XV International Conference on Atmospheric Electricity, Norman, OK, USA, 15–20 June 2014; pp. 15–20.
28. Moura, R.A.; Schroeder, M.A.; Menezes, P.H.; Nascimento, L.C.; Lobato, A.T. Influence of the soil and frequency effects to evaluate atmospheric overvoltages in overhead transmission line—Part II: The influence of the soil in atmospheric overvoltages. In Proceedings of the XV International Conference on Atmospheric Electricity, Norman, OK, USA, 15–20 June 2014; pp. 15–20.
29. De Conti, A.; Emídio, M.P.S. Extension of a modal-domain transmission line model to include frequency-dependent ground parameters. *Electr. Power Syst. Res.* **2016**, *138*, 120–130. [CrossRef]
30. Li, Z.; He, J.; Zhang, B.; Yu, Z. Influence of frequency characteristics of soil parameters on ground-return transmission line parameters. *Electr. Power Syst. Res.* **2016**, *139*, 127–132. [CrossRef]
31. Martins-Britto, A.G.; Lopes, F.V.; Rondineau, S.R.M.J. Multilayer earth structure approximation by a homogeneous conductivity soil for ground return impedance calculations. *IEEE Trans. Power Deliv.* **2019**, *35*, 881–891. [CrossRef]
32. Tsiamitros, D.A.; Papagiannis, G.K.; Dokopoulos, P.S. Homogenous Earth Approximation of Two-Layer Earth Structures: An Equivalent Resistivity Approach. *IEEE Trans. Power Deliv.* **2007**, *22*, 658–666. [CrossRef]
33. Zanon, F.O.; Leal, O.E.; De Conti, A. Implementation of the universal line model in the alternative transients program. *Electr. Power Syst. Res.* **2021**, *197*, 107311. [CrossRef]
34. Martinez-Velasco, J.A. *Power System Transients: Parameter Determination*; CRC Press: Boca Raton, FL, USA, 2009; p. 644.
35. Sunde, E.D. *Earth Conduction Effects in Transmission Systems*; Dover Publications Inc.: New York, NY, USA, 1968.
36. Salvador, J.P.L.; Alipio, R.; Lima, A.C.S.; Correia de Barros, M.T. A Concise Approach of Soil Models for Time-Domain Analysis. *IEEE Trans. Electromagn. Compat.* **2020**, *62*, 1772–1779. [CrossRef]
37. Manjunath, A.D.B.; Khan, F.; Noyanbayev, N.; Harid, N.; Griffiths, H.; Nogueira, R.P.; De Oliveira, N.T.C.; Haddad, M.; Ramanujam, S. Investigation Into Variation of Resistivity and Permittivity of Aqueous Solutions and Soils With Frequency and Current Density. *IEEE Trans. Electromagn. Compat.* **2021**, 1–13. [CrossRef]
38. Portela, C. Measurement and modeling of soil electromagnetic behavior. In Proceedings of the 1999 IEEE International Symposium on Electromagnetic Compatibility. Symposium Record (Cat. No. 99CH36261), Seattle, WA, USA, 2–6 August 1999; IEEE Volume 2, pp. 1004–1009.
39. Friedman, S.P. Soil properties influencing apparent electrical conductivity: A review. *Comput. Electron. Agric.* **2005**, *46*, 45–70. [CrossRef]
40. Longmire, C.L.; Longley, H.J. *Time Domain Treatment of Media with Frequency-Dependent Electrical Parameters*; MRC-N-1, DNA F; Mission Research Corporation: Santa Barbara, CA, USA, 1973; Volume 3167.
41. Longmire, C.; Smith, K. *A Universal Impedance for Soils, Topical Report for Period July 1–September 30*; Defense Nuclear Agency: Santa Barbara, CA, USA, 1975.
42. Scott, J.H. *Electrical and Magnetic Properties of Rock and Soil*; Theoretical Notes, Note 18; U. S. Geological Survey: Reston, VA, USA, 1966. Available online: http://ece-research.unm.edu/summa/notes/TheoreticalPDFs/TN018.pdf (accessed on 12 January 2022).
43. Messier, M. *The Propagation of an Electromagnetic Impulse through Soil: Influence of Frequency Dependent Parameters*; Tech. Rep. MRC-N-415; Mission Res. Corp.: Santa Barbara, CA, USA, 1980.
44. Messier, M. *Another Soil Conductivity Model*; Internal Rep.; JAYCOR: Santa Barbara, CA, USA, 1985.
45. Ramos-Leaños, O.; Naredo, J.L.; Gutierrez-Robles, J.A. An advanced transmission line and cable model in MATLAB for the simulation of power-system transients. In *MATLAB: A Fundamental Tool for Scientific Computing and Engineering Applications*; InTech: Shanghai, China, 2012; pp. 269–304.
46. Wedepohl, L.M.; Nguyen, H.V. Frequency-dependent transformation matrices for untransposed transmission lines using newton-raphson method. *IEEE Trans. Power Syst.* **1996**, *11*, 1538–1546. [CrossRef]
47. Chrysochos, A.I.; Papadopoulos, T.A.; Papagiannis, G.K. Robust Calculation of Frequency-Dependent Transmission-Line Transformation Matrices Using the Levenberg–Marquardt Method. *IEEE Trans. Power Deliv.* **2014**, *29*, 1621–1629. [CrossRef]
48. Tavares, M.C.; Pissolato, J.; Portela, C.M. Mode domain multiphase transmission line model-use in transient studies. *IEEE Trans. Power Deliv.* **1999**, *14*, 1533–1544. [CrossRef]
49. Moreno, P.; Ramirez, A. Implementation of the Numerical Laplace Transform: A Review Task Force on Frequency Domain Methods for EMT Studies, Working Group on Modeling and Analysis of System Transients Using Digital Simulation, General Systems Subcommittee, IEEE Power Engineering Society. *IEEE Trans. Power Deliv.* **2008**, *23*, 2599–2609. [CrossRef]
50. Seppanen, J.M.; Tammi, P.O.; Haarla, L.C. Underground ground wires for transmission lines: Electrical behavior and feasibility. *IEEE Trans. Power Deliv.* **2012**, *28*, 206–215. [CrossRef]
51. Kurokawa, S.; Filho, J.; Tavares, M.; Portela, C.; Prado, A. Behavior of overhead transmission line parameters on the presence of ground wires. *IEEE Trans. Power Deliv.* **2005**, *20*, 1669–1676. [CrossRef]
52. Torrez Caballero, P. Inclusion of the Frequency Dependence in the Bergeron Model: Representation of Short and Long Transmission Lines Considering Electromagnetic Transients Resulting from Switching Operations and Lightning Strikes. Ph.D. Thesis, São Paulo State University, Ilha Solteira, Brazil, 2018.

53. Wang, D.; Hou, M.; Guo, Y. Travelling Wave Fault Location of HVAC Transmission Line Based on Frequency-Dependent Characteristic. *IEEE Trans. Power Deliv.* **2021**, *36*, 3496–3505. [CrossRef]
54. Terespolsky, B.R.; Nixon, K.J. Developing an approximation to the heidler function-with an analytical transformation into the frequency domain. In Proceedings of the 2014 International Conference on Lightning Protection (ICLP), Shanghai, China, 11–18 October 2014; pp. 1326–1330.
55. Terespolsky, B.R. An Approximation to the Heidler Function with an Analytical Integral for Engineering Applications Using Lightning Currents. Ph.D. Thesis, Faculty of Engineering and the Built Environment, School of Electrical and Information Engineering, University of the Witwatersrand, Joanesburgo, South Africa, 2015.
56. Andreotti, A.; Falco, S.; Verolino, L. Some integrals involving Heidler's lightning return stroke current expression. *Electr. Eng.* **2005**, *87*, 121–128. [CrossRef]
57. Feizhou, Z.; Shanghe, L. A new function to represent the lightning return-stroke currents. *IEEE Trans. Electromagn. Compat.* **2002**, *44*, 595–597. [CrossRef]
58. Heidler, F.; Cvetić, J. A class of analytical functions to study the lightning effects associated with the current front. *Eur. Trans. Electr. Power* **2002**, *12*, 141–150. [CrossRef]
59. Delfino, F.; Procopio, R.; Rossi, M.; Rachidi, F. Prony series representation for the lightning channel base current. *IEEE Trans. Electromagn. Compat.* **2011**, *54*, 308–315. [CrossRef]
60. Vujevic, S.; Lovric, D.; Balaz, Z. Numerical approximation of the lightning current function. In Proceedings of the SoftCOM 2009—17th International Conference on Software, Telecommunications & Computer Networks, Split, Croatia, 17–19 September 2009; pp. 19–23.